Analysis of Refractive Effects on Mid-Latitude SuperDARN Velocity Measurements

Kristoffer Charles Dixon

Thesis submitted to the faculty of the Virginia Polytechnic Institute and State University
in partial fulfilment of the requirements for the degree of

Master of Science
in
Electrical Engineering

J. Michael Ruohoniemi, Chair
Joseph B. H. Baker, Co-Chair
Robert McGwier
R. Michael Buehrer

September 25,2014
Blacksburg, Virginia

Keywords: SuperDARN, mid-latitude, ionosphere, propagation

Analysis of Refractive Effects on Mid-Latitude SuperDARN Velocity Measurements

Kristoffer Charles Dixon

(ABSTRACT)

First time ionospheric refractive index values have been determined at mid latitudes using frequency switched SuperDARN plasma convection velocity estimates. Previous works have found a disparity between high latitude SuperDARN plasma convection velocities and those made by other devices. It was noted that the scattering volume's refractive index was being neglected when estimating plasma convection velocities, meaning a correction factor was needed in order to more accurately reflect other measurements. Later work proposed a solution which implemented frequency switching in SuperDARN radars and determined a single correction factor based off of many years of data. We present case study driven research which applies the principles of these previous works to mid latitudes in an attempt to determine the refractive effect in mid latitude SuperDARN plasma convection velocity data by examining frequency switched quiet time ionospheric scatter. It was found that the 1/2 hop ionospheric scatter exhibited little to no measurable refractive effect ($n \sim 1$), while the 1 1/2 hop ionospheric scatter tended to exhibit measurable refractive effects ($n \sim 0.7$). This is then expanded to a storm-time 1/2 hop ionospheric scatter case study. It was again found that the refractive effects were nearly negligible ($n \sim 1$), indicating that the 1/2 hop plasma convection velocities reported by mid latitude SuperDARN radars only require a very small correction factor, if any at all.

Acknowledgments

First and foremost I would like to thank my advisors Dr. Joseph Baker and Dr. Mike Ruohoniemi for giving me an opportunity to pursue this work at Virginia Tech, and for their countless hours of guidance and support. I would also like to thank the Ted and Karyn Hume Center for National Security and Technology, especially Dr. Bob McGwier, for funding me and opening doors within the defence community. Thank you to Dr. Mike Buehrer for teaching some of the most interesting and engaging classes available at Virginia Tech. And lastly, thank you to Dr. Bill Bristow at the University of Alaska Fairbanks for getting me into the SuperDARN community in the first place.

I would like to thank my family for their support on this insane adventure and loving me all the way from Alaska. I would like to thank my friends, especially those in Illinois and Texas, for putting up with my complaining and making me a Peggle champion.

Finally, I want to thank Matt for giving me a place to stay. Yee.

Contents

List of Figures

List of Tables

Chapter 1

Introduction

1.1 The Ionosphere

The Earth is enveloped by a gaseous atmosphere dominated by nitrogen and oxygen and can be vertically divided into regions based on its temperature profile. The four principle regions of this profile in ascending order are the troposphere, the stratosphere, the mesosphere, and the thermosphere. Although the stratosphere tends to exhibit a net increase in temperature with altitude, the cumulative trend of the three bottom layers is a net decrease. However at approximately 80 km there is a temperature inversion, marking the beginning of the thermosphere. This increase in temperature with altitude is the result of ionizing solar radiation (e.g., ultraviolet and X-ray emissions from the sun) being absorbed by the local atmosphere, ionizing neutral particles and forming a weakly ionized plasma [*Rishbeth and Garriott*, 1969]. The region of the atmosphere in which this weakly ionized plasma exists is known as the ionosphere [*Kelley*, 2009]. Above 600 km temperatures again begin to drop marking the beginning the Earth's outermost region, the exosphere.

Figure 1.1 illustrates a typical electron density profile for both daytime (solid line) and nighttime (dashed line) conditions. The vertical regions of Earths ionosphere can be divided into three principal layers based on the vertical electron density profile:

- **The D-region** (50 km - 90 km): The lowest layer of the ionosphere, the D-region,

is typically only present during daytime conditions due to the high degree of recombination. Without sunlight to maintain ionization, these ions quickly recombine and the region dissipates. The dominate ion species is NO^+, though N_2^+ and O_2^+ may be present. The D-region is primarily responsible for high frequency (HF) radio wave absorption and may even completely restrict shortwave radio usage during Polar Cap Absorption (PCA) events, though these are rare.

- **The E-region** (90 km - 150 km): The middle layer of the ionosphere, the E-region, is present during both daytime and nighttime conditions, though the height typically increases during nighttime conditions. The dominate ion species are NO^+ and O_2^+. Sporadic highly ionized layers may appear in the E-region and facilitate skywave propagation up to a few hundred megahertz.

- **The F-region** (above 150 km): The top layer of the ionosphere, the F-region, is usually the densest region of the ionosphere. It exists in both daytime and nightime conditions, and daytime conditions often create two peaks in the F-region electron density profile, dividing the F-region further into the F1 and F2 layers. The peak density occurs near 250 km during daytime and near 300 km during night. At this peak altitude the dominate ion species is O^+. The F-region is the principle facilitator of HF skywave propagation [*Kelley*, 2009].

Photoionization is not the only generator of the ionosphere. The solar wind is a constant stream of supersonic collisionless plasma radiating in all directions from the sun. These charged particles carry a remnant of the sun's magnetic field named the Interplanetary Magnetic Field (IMF). The solar wind's interaction with the Earth's magnetic field is the key driver for many ionospheric phenomena, especially those in the high-latitude ionosphere (the aurora is a good example), and is heavily influenced by magnetic reconnection as illustrated

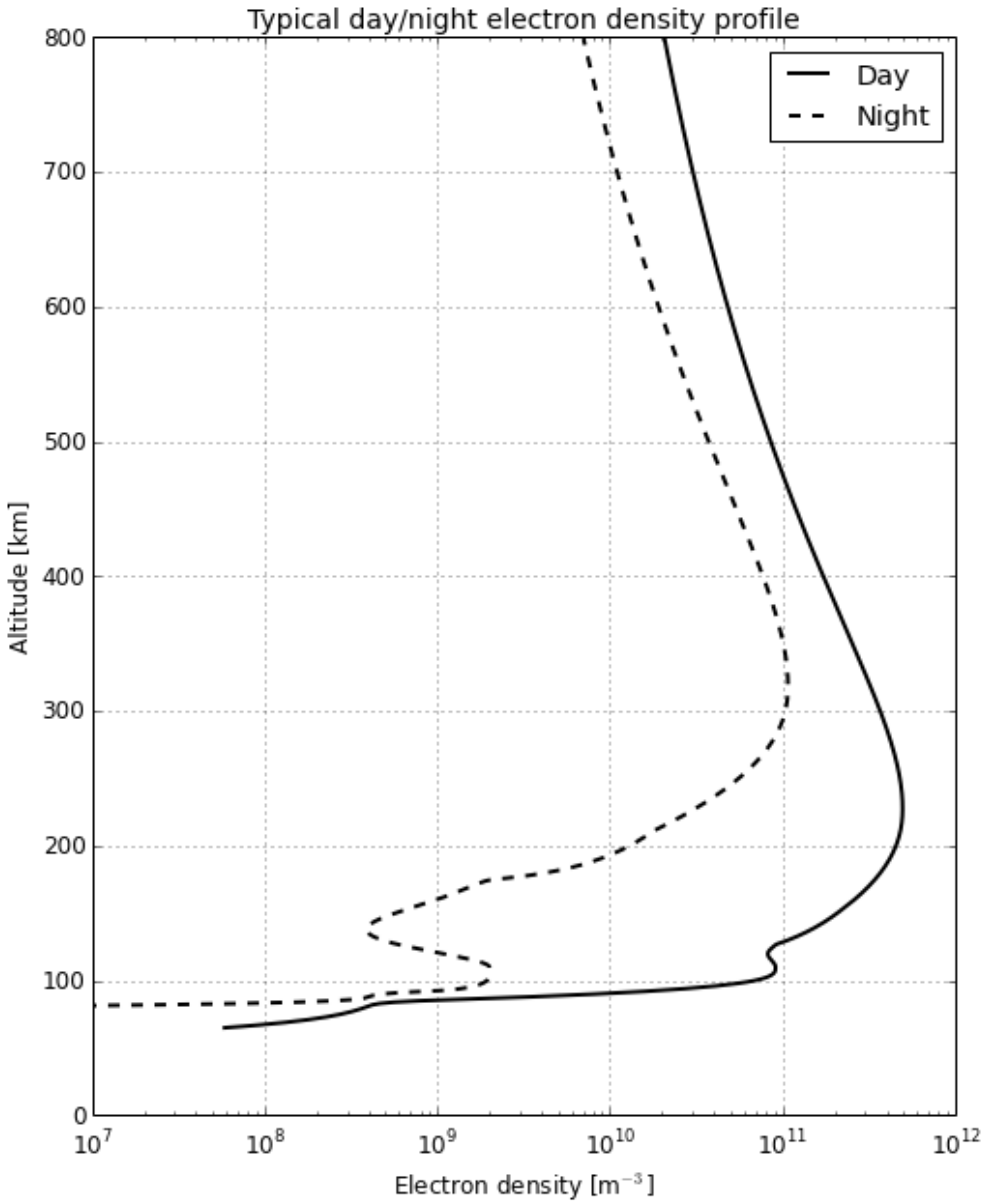

Figure 1.1: Simulated vertical day/night electron density profile in the ionosphere using the International Reference Ionosphere. Daytime ionization causes electron densities to increase significantly and to form additional layers.

in Figure 1.2. At about 14 R_E a feature named the bow shock forms which slows the solar wind to subsonic speeds. This region of subsonic flow is named the magnetosheath. As the solar wind encounters the Earth's magnetosphere, it compresses the dayside magnetosphere. Conversely, the solar wind creates an elongated geomagnetic tail on the nightside. The boundary at which the solar wind encounters the Earth's magnetosphere is named the magnetopause. Behind the magnetopause exists Earth's geomagnetic field. Due to the orientation of the IMF relative to Earth's geomagnetic field, one end of the IMF can connect to a terrestrial field line while the other stretches out into space. This connection allows for solar particles to move Earthward along these conductive field lines into Earth's ionosphere, seeding many ionospheric phenomena such as the aurora borealis [*"Kivelson and Russell*, "1995"].

The ionosphere is an incredibly dynamic, stochastic system. Due to the cyclic nature of this system (e.g. the diurnal day/night cycle, the yearly solar cycle, and the solar minimum/maximum cycle), plasma density values are constantly in flux and are strongly driven by solar activity. A period of great solar activity is typically referred to as a stormy period while a period of general quiescence is referred to a quiet period. Within the ionosphere, structures tend to appear with electron densities fluctuating above background plasma levels that are usually the result of some kind of plasma instability. The spatial scale of these structures varies greatly, ranging from many kilometers down to only a few centimeters. In the F-region ionosphere, horizontal drift of these plasma density irregularities tends to be the result of the motion of the background plasma. These structures and their importance to this research are discussed in future sections.

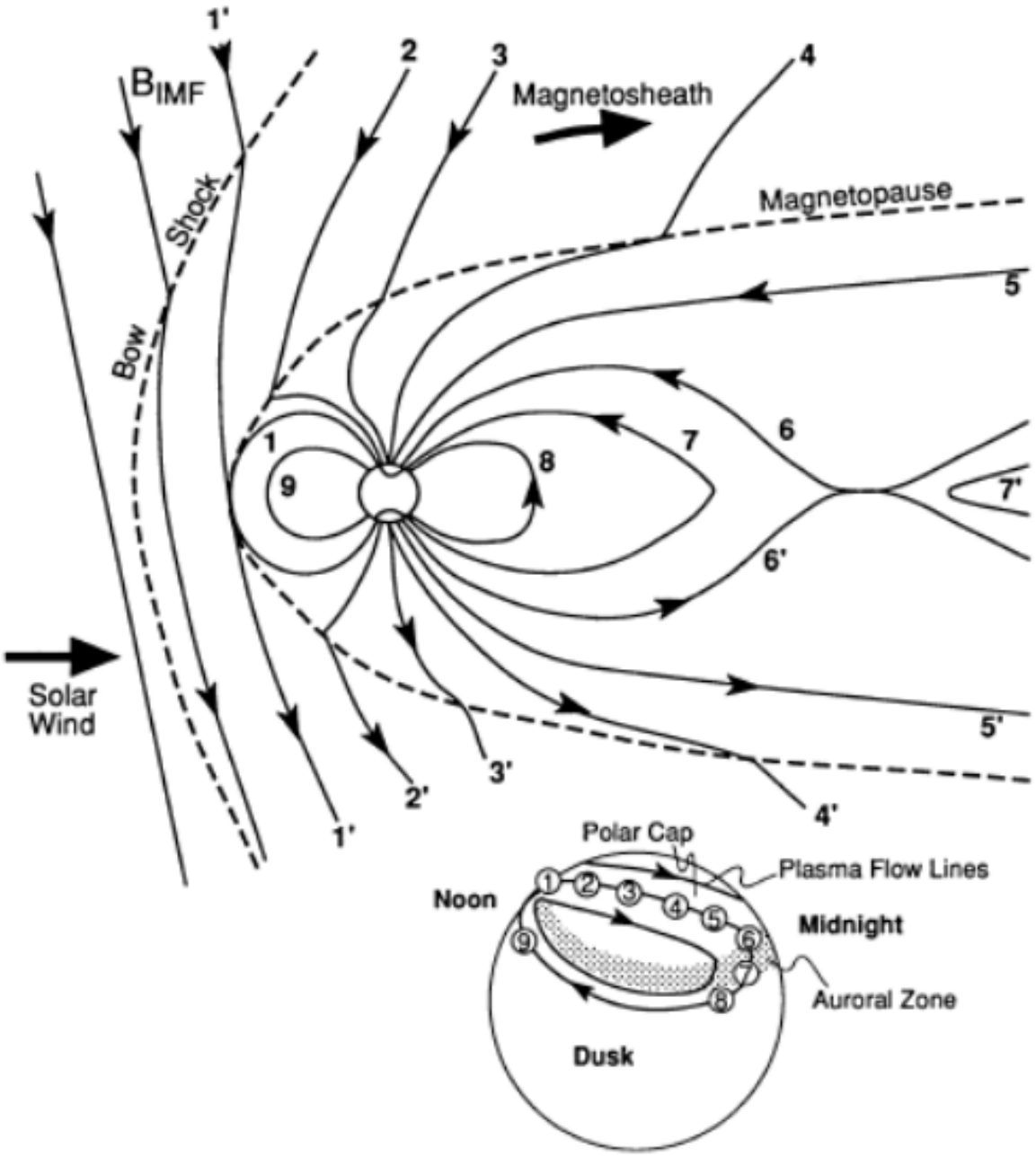

Figure 1.2: Illustration of magnetic reconnection. Numbered IMF field lines show the process of IMF lines encountering the magnetosphere, being "bent" around the magnetosphere, and ultimately becoming connected to the Earth's geomagnetic field. Taken from M. G. Kivelson and C. T. Russell. *Introduction to Space Physics*. Cambridge atmospheric and space science series. Cambridge University Press, 1995. ISBN 9780521457149. Used under fair use, 2014.

1.2 Radar

Radar, an acronym for **RA**dio **D**etection **A**nd **R**anging, is a remote sensing technique which uses electromagnetic radiation to discern conditions and illuminate features of the environment. Typical radar systems emit electromagnetic radiation in a angularly limited beam which may scatter off reflecting features, returning to the radar as an echo after some time. These echoes, along with knowledge of beam position, allow for the radar system to measure an object's azimuth, elevation, range, and speed relative to the radar. More advanced systems may also extrapolate an objects size, shape, reflectivity, and rotation [*Skolnik*, 2008].

A pulse-doppler radar system is a system which emits short pulses of electromagnetic radiation in order to determine range and velocity. The pulse-to-echo time T can be used to determine range R via the relationship

$$R = \frac{cT}{2}. \tag{1.1}$$

The line-of-sight (LOS) velocity v can be calculated by examining the Doppler shift f_D imposed on the pulse and the radar operating wavelength λ via the relationship

$$v = \frac{f_D \lambda}{2}. \tag{1.2}$$

A radar system usually must update its knowledge of a scene by sending out pulses at a defined rate, known as the pulse repetition frequency (PRF). Ambiguities arise in both range and time due to the choice of PRF. A range return becomes ambiguous if it returns to the radar after the next pulse has launched, causing the radar to interpret the return as being

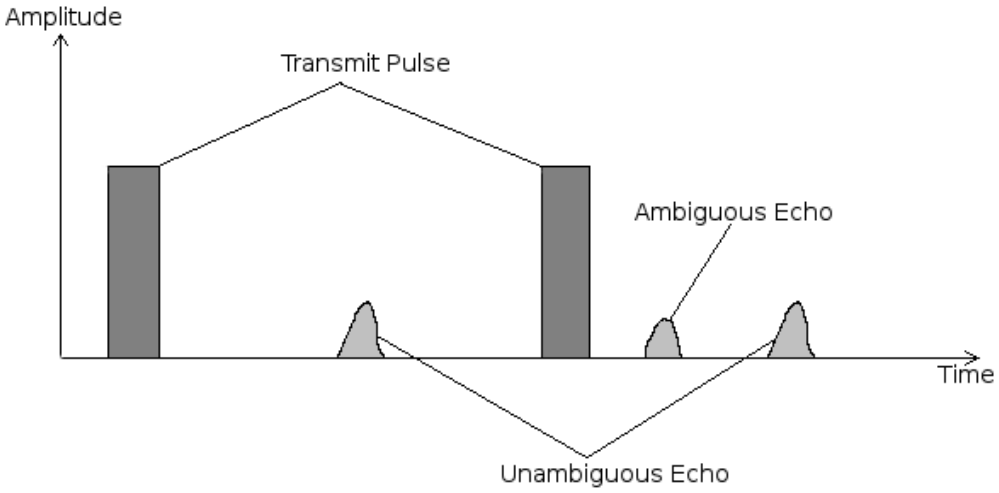

Figure 1.3: An example of an ambiguous echo. Both the unambiguous echoes occur after some time for both transmitted pulses but the ambiguous echo arrives at the receiver after the next pulse is launched, causing the radar to interpret a target much closer than it actually is.

much closer than it actually is as shown in Figure 1.3. A velocity return becomes ambiguous when the measured Doppler shift exceeds PRF, causing the Doppler shift to be measured incorrectly. Both the maximum unambiguous range R_{ua} and the maximum unambiguous velocity v_{ua} are both defined by the PRF and can be expressed as

$$R_{ua} = \frac{c}{2PRF} \tag{1.3}$$

and

$$v_{ua} = \pm\frac{\lambda PRF}{4}. \tag{1.4}$$

Both these equations demonstrate a common theme in radar: ambiguity. Another kind of ambiguity which will be explored in this research is ambiguity due to refraction in HF radar.

1.3 Refraction and HF Propagation

Refraction occurs when a propagating wave obliquely encounters a boundary with two unequal impedances. The change in impedance changes the velocity of propagation, which ultimately bends the wave due to the wave's phase front encountering the boundary at different times. The degree of bending is proportional to both the ratio of the impedances and the entrance angle. This relationship is known as Snell's Law and is written as

$$\frac{n_1}{n_2} = \frac{\sin\theta_2}{\sin\theta_1}, \tag{1.5}$$

where θ indicates the entrance/exit angle (taken with respect to the normal to the boundary) and n indicates the media's refractive indices. In many cases, it is convenient to consider the impedance Z of a medium in terms of it's relationship to the impedance of freespace Z_0, where impedance is the ratio of a material's permeability to permittivity

$$Z = \sqrt{\frac{\mu}{\epsilon}}, \tag{1.6}$$

where μ is the material's permeability and ϵ is the material's permittivity. This relationship of Z/Z_0 is known as a materials refractive index. Because a material's impedance tends to be frequency dependant, a material's refractive index tends to also be frequency dependant. Another way of representing refractive index is the ratio of the speed of light in a vacuum c (usually referred to as the "speed of light") to the wave's phase velocity v_p as shown in Equation 1.7.

$$n = \frac{c}{v_p} \tag{1.7}$$

In most cases the refractive index n of a medium is greater than unity, though in some rarer scenarios it may be less than unity (e.g., light waves in glass). In the cases where a medium's refractive index is less than unity, while the phase velocity v_p is technically propagating faster than the speed of light c, the group velocity v_g is not, meaning that nothing in the system is actually propagating faster than the speed of light c.

One scenario where $n < 1$ is in a weakly ionized plasma such as the ionosphere for which increased electron densities result in decreased refractive indices. The solution of the refractive index of the ionosphere tends to be associated with Sir Edward Appleton and can be expressed in a simplified form as

$$n = \sqrt{1 - \frac{N_e e^2}{\epsilon_0 m \omega^2}} \tag{1.8}$$

where N_e is the electron density per cubic meter, e is the charge of an electron, ϵ_0 is the permittivity of freespace, m is the electron mass, and ω is the angular wave frequency. Equation 1.8 assumes that collisions between particles are are rare, allowing for ionized particles to exist for relatively long periods of time. The plasma related components in Equation 1.8 represent the plasma's natural charge density oscillation and can be expressed as

$$w_p = \sqrt{\frac{N_e e^2}{\epsilon_0 m}}. \tag{1.9}$$

The quantity w_p in Equation 1.9 is generally referred as the radial plasma frequency of a plasma. By combining 1.9 and 1.8, an expression relating plasma frequency f_p to wave frequency f may be found and can be expressed as

$$n_s = \sqrt{1 - f_p^2/f^2}. \tag{1.10}$$

In the F-region ionosphere it is not uncommon to observe plasma frequencies between 1 MHz and 10 MHz.

The refractive index properties of the ionosphere may be exploited for special propagation modes using electromagnetic radiation at HF band frequencies. At this range of frequencies, HF waves propagating obliquely to the ionosphere may experience refraction to the point of "bouncing" back down to Earth's surface, known as skywave propagation, allowing for signals to be received from many thousands of kilometers away. An illustration of this is presented in Figure 1.4. A ray propagates from the transmitter and refracts back to Earth. The maximum height of this ray is slightly ambiguous due refraction, but the virtual height (the maximum height if the ray were simply reflected) of this ray gives a good approximation. In the case of HF radar, the virtual path and the actual path have the same time delay, making it difficult to measure the ray's actual height. This long range communication technique was pioneered at the turn of the 20th century by Guglielmo Marconi and is still used today.

The refraction of HF waves in the ionosphere also allows for scientific instruments to examine space weather conditions. One such instrument, an ionosonde, measures the frequency dependent nature of the ionosphere by sweeping through a wide bandwidth of transmitting frequencies. This technology dates back to physicists Gregory Breit and Merle Tuve in the 1920s. Another instrument, HF radar systems, study the ionosphere by scattering off of field aligned plasma density irregularities and have been around since at least the 1960s [*Bates*, 1966]. One such HF radar system, known as SuperDARN, constantly monitors mid-latitude, high-latitude, and auroral plasma convections at E- and F-region altitudes.

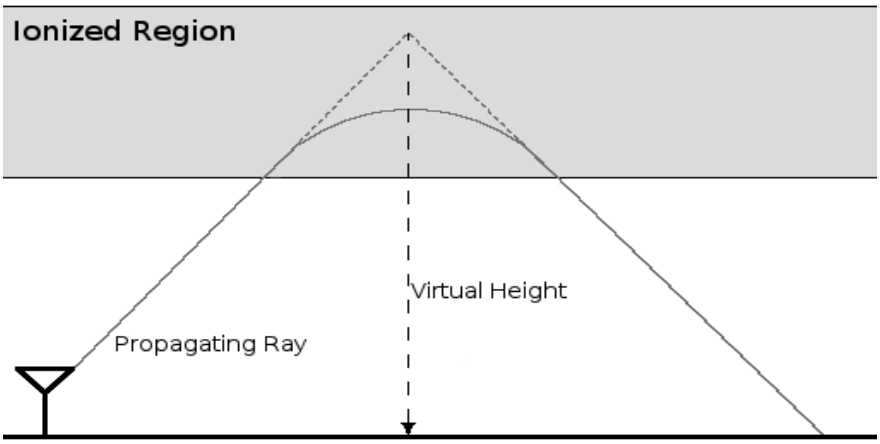

Figure 1.4: An illustration of skywave propagation. A ray is refracted by the ionosphere back down to the Earth. The actual height this ray achieves becomes a bit ambiguous, but the virtual height gives a good approximation.

1.4 SuperDARN

The Super Dual Auroral Radar Network (SuperDARN) is a continually growing international chain of ground-based HF coherent scatter radars that have been monitoring decameter-scale irregularities in the high-latitude F-region ionosphere for approximately 20 years [*Greenwald et al.*, 1995]. More recently, a chain of SuperDARN radars has been added in order to monitor the mid-latitude ionosphere. The SuperDARN network in the northern hemisphere currently consists of 21 active radars, 9 of which monitor the mid-latitude ionosphere. An image containing all active SuperDARN radars in both the southern and nothern hemisphere is included in Figure 1.5. The international chain of SuperDARN radars is managed by many institutes which encourage data sharing and collaborative efforts [*Chisham et al.*, 2007].

SuperDARN radars incorporate a main linear array of antennas which allow for the

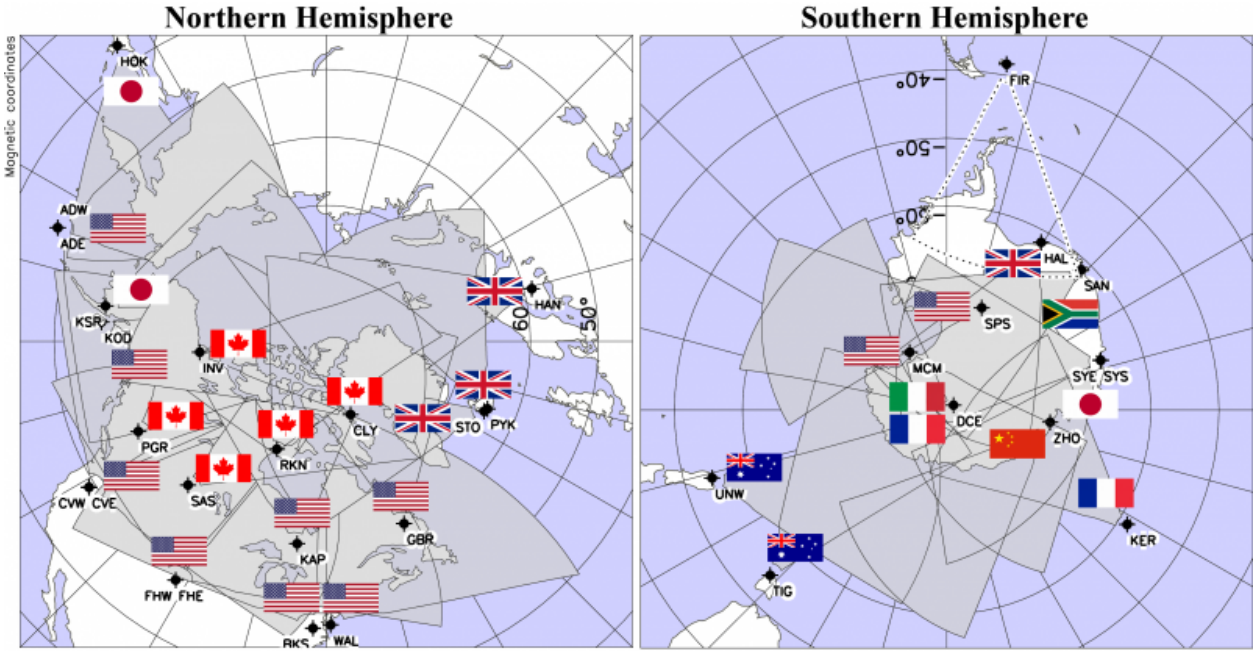

Figure 1.5: All active SuperDARN radars for both the southern and northern hemispheres and their international ownership. More radars are planned for the future as the need for more ionospheric sensing systems increases.

phasing of 16 to 24 unique beam positions separated primarily in azimuth. They typically perform a complete azimuthal scan every one to two minutes. For the periods considered in this study, the Blackstone SuperDARN radar had a total scan time $\Delta t = 60$ seconds. Each beam dwell typically operates with a 45 km range resolution and contains 75 to 100 unique range bins. The physical structure of a SuperDARN antenna consists of a main array of 16 radiating elements. Each element is typically either a log-periodic antenna or a twin-terminated folded dipole antenna. Each element emits approximately 300 watts of power yielding a combined power of 4.8 kW which is relatively low compared to many radar systems of a similar size. Each radar also has a 4 element interferometer array behind the main array which allows for angle of arrival measurement on the receive side [*Greenwald et al.*, 1995].

SuperDARN radars primarily observe echoes from two main scattering sources. Ground

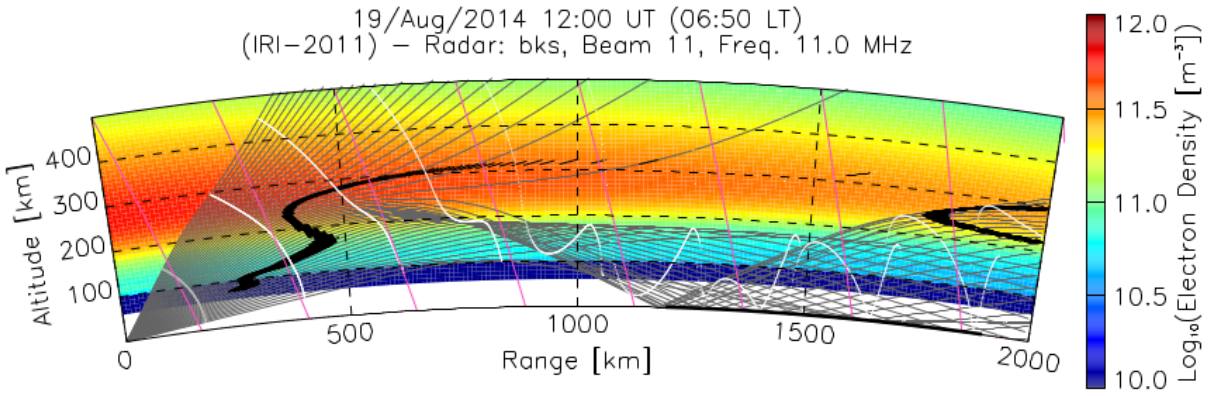

Figure 1.6: An illustration of raytracing performed for the Blackstone SuperDARN radar. Gray lines indicate ray paths. Black points indicate points of scatter (either from orthogonality with pink magnetic field lines or from the ground). White points indicate constant phase fronts. This illustration is a good example of 1/2 hop scatter, ground scatter, and 1 1/2 hop scatter.

scatter generally occurs when a wave is refracted back down to the earth by the ionosphere and strikes the earth's surface, returning to the radar typically along the same propagation path. Ionospheric scatter occurs when a wave is reflected by some scattering source in the ionosphere and returns to the radar. Scatter from the ionosphere generally occurs when a wave is refracted to the point of near-perpendicularity with magnetic field lines and encounters some scattering structure. If decameter-scale plasma irregularities are present and aspect conditions are met, Bragg scattering can occur and coherent backscatter may be observed [*Tsunoda*, 1988]. A third scatter type occurs from quickly dissipating trails of ionization left by meteors entering the ionosphere. This particular scatter type, named "meteor scatter", is not of importance for this research.

SuperDARN ionospheric scatter can generally be grouped into categories based on their propagation path: 1/2 hop scatter and 1 1/2 hop scatter. Hop generally refers to energy bouncing off of the Earth and returning to the ionosphere. The 1/2 hop scatter scenarios occur when energy is launch from a SuperDARN radar, scatters off some structure in the

ionosphere, and returns to the radar without being reflected off the ground. The 1 ½ hop scatter scenarios occur when energy is launched from a SuperDARN radar, refracted back down to the Earth, reflect off of the Earth, and ultimately scatter off of the structure in the ionosphere. ½ hop scatter almost always occurs much closer to the radar than 1 ½ hop scatter. An example of these propagation paths are presented in Figure 1.6. The plot in Figure 1.6 is a raytracing simulation and depicts rays being launched from various launch angles from a SuperDARN radar into the ionosphere. The color gradients depict the electron density profile of an IRI model ionosphere. Gray lines indicate propagating rays with white markers indicating the constant phase fronts. Pink lines illustrate the magnetic field orientation and black hatching identify areas where scatter may be present (both scattering from near-orthogonality with magnetic field lines and from the Earth's surface). The plot shows an initial grouping of ½ hop ionospheric scatter as well as a further grouping of 1½ hop ionospheric scatter. Note that some higher launch angles penetrate the ionosphere with no chance of scatter back to the radar.

Another example of these two types of ionospheric scatter is presented in Figure 1.7 in the form of two azimuthal scans or field-of-view (FOV) plot for the Blackstone SuperDARN radar. Colors indicate measured LOS velocities that have been binned into discrete 45 km range bins. Note the absence of 1 hop ground scatter in the left most plot. Both these plots illustrate observations of plasma convection in the ionosphere.

Plasma convection observations in the night-time ionosphere made by mid-latitude SuperDARN radars tends to come from the slow moving westward $\mathbf{E}\times\mathbf{B}$ plasma drift generated by poleward directed electric fields named Sub Auroral Ionospheric Scatter (SAIS) [*Ribeiro et al.*, 2012]. Abnormal events consisting of narrow streams fast moving westward flow may occur just below the auroral zone and are typically named either a subauroral ion drift (SAID) [*Spiro et al.*, 1979] or a subauroral polarization stream (SAPS) [*Foster and Burke*,

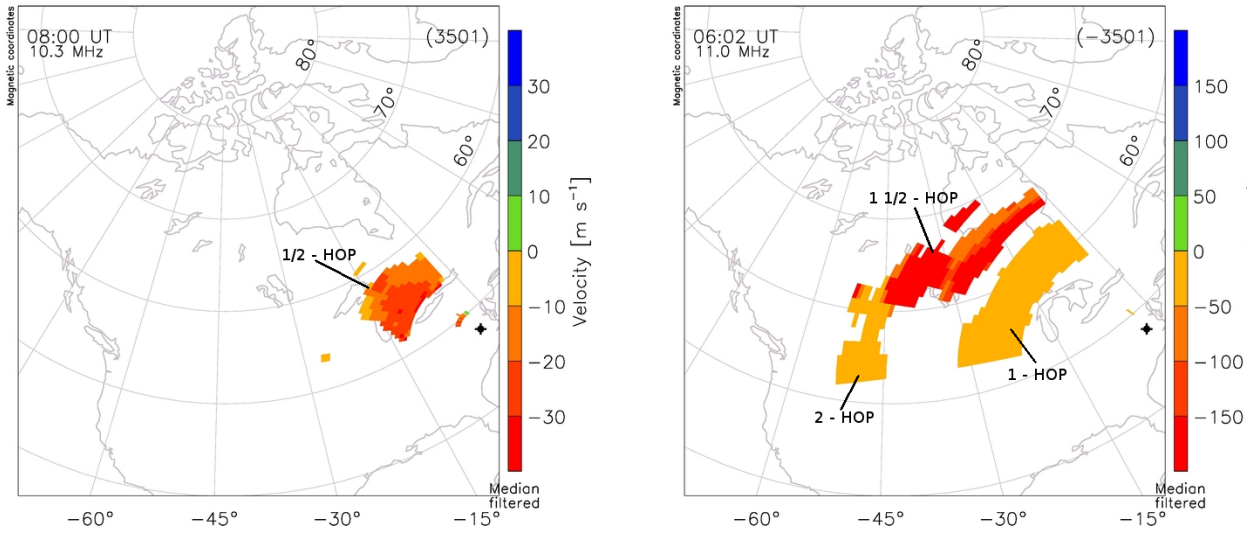

Figure 1.7: Azimuthal scans demonstrating the field-of-view of the Blackstone SuperDARN radar in Blackstone, Virginia. The left plot (12/27/2013) shows typical scatter from a 1/2 hop ionospheric scatter scenario while the right plot (4/17/2014) shows typical scatter from a 1 1/2 hop ionospheric scatter scenario. Note that the 1/2 hop scatter scenario (left) exhibits very low velocities and has no ground scatter present, while the 1 1/2 hop scatter scenario (right) exhibits very high velocities and has noticable 1 hop and 2 hop ground scatter bands.

2002]. These events are rare and are not a focus of this study. Auroral zone scatter is also visible, though usually only under 1 1/2 hop scatter conditions.

1.5 Convection Velocity Underestimation

SuperDARN radars exploit the refractive effects of the ionosphere on HF waves to achieve scattering which alters relationship between measured LOS velocities and actual LOS plasma convection velocities. This effect has been explored at high latitudes and described by this expression [*Gillies et al.*, 2011]

$$v_m = n_s v_c. \tag{1.11}$$

where v_m is the measured SuperDARN LOS velocity and v_c is the actual LOS component

of the plasma convection velocity. The relationship in Equation 1.11 indicates that these velocities are linearly proportional to the degree of refraction experienced.

Previous studies performed at high-latitudes found that measured SuperDARN LOS plasma convection velocity estimates tended to be lower than other instrument measurements, sometimes by as much as 20% [*Xu et al.*, 2001; *Drayton et al.*, 2005]. Results from *Xu et al.* [2001] are presented in Figure 1.8 and show a disparity between DMSP satellite plasma convection velocities and those measured by SuperDARN radars. It has been suggested that LOS velocities calculations are in error due to neglecting the refractive index of the scattering volume n_s [*Gillies et al.*, 2009]. Because the radar wave group velocity is less than c in the ionosphere, reported Doppler frequency shift measurements are underestimated. A correction factor would need to be applied to previous velocity values in order to more accurately reflect other measurements.

Several methods have been proposed to estimate the refractive index of the scattering volume using SuperDARN radars at high latitudes. One method uses angle-of-arrival data as a proxy to determine refractive index and assumes the ionosphere is spherically stratified [*Gillies et al.*, 2009]. Because this assumption does not always hold, it does not give the most accurate results for refractive index. Another method uses the IRI model to infer electron density values, thus giving an estimated refractive index at the spatial and temporal location of the populated SuperDARN range bin [*Ponomarenko et al.*, 2009]. This method does not take into account small-scale irregularities that SuperDARN radars so often observe due to the IRI model's large time-scale focus. While a decent improvement, the corrected velocities from these studies were still on average lower when compared to DMSP satellite velocities.

A more recent method was proposed by [*Gillies et al.*, 2011] which suggested using a frequency-switched mode of operation in SuperDARN radars. Substituting the simplified O-mode Appleton-Hartree equation presented in Equation 1.10 into Equation 1.11 yields

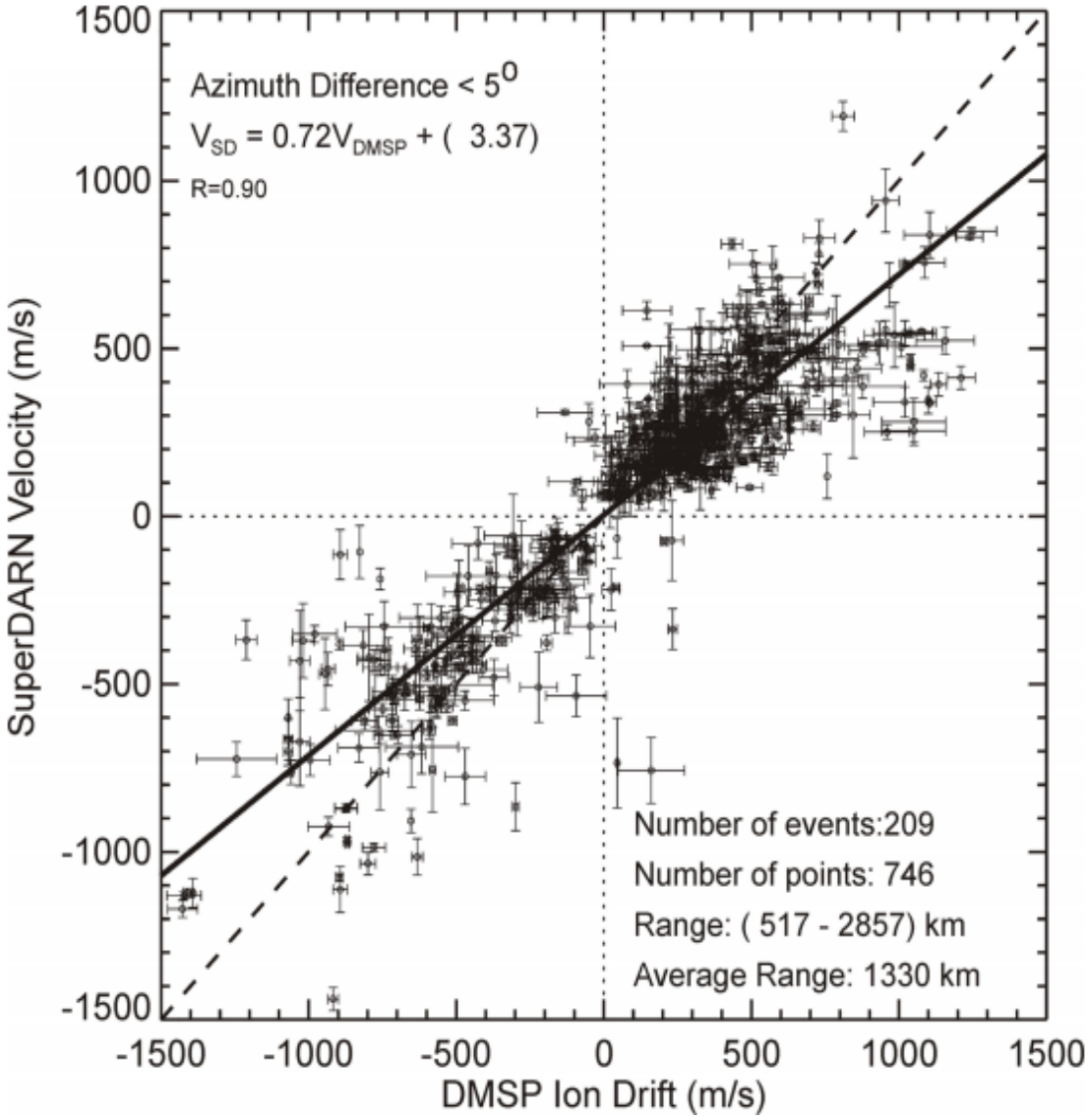

Figure 1.8: A comparison of SuperDARN and DMSP satellite plasma convection velocities. The plot shows a general disagreement between the two datasets with the SuperDARN data being on average 20% lower. Taken from L. Xu, A. V. Koustov, J. Thayer, and M. A. McCready. Superdarn convection and sondrestrom plasma drift. *Annales Geophysicae*, 19(7):749-759, 2001. doi 10.5194/angeo-19-749-2001. Used under fair use, 2014.

the frequency dependant equation for velocity, written as

$$v_m = v_c\sqrt{1 - \frac{f_p^2}{f^2}}. \tag{1.12}$$

Inspection of Equation 1.12 reveals to two unknowns, f_p and v_c. Using the assumption that f_p and v_c are relative constant before and after a frequency switch, the velocity measurement before the switch (v_{m1}) and the velocity measurement after the switch (v_{m2}), as well as the frequency before the switch (f_1) and after the switch (f_2), can be used to find a solution for f_p and v_c. The solution for the volume's plasma frequency f_p then takes the form of

$$f_p^2 = \frac{f_1^2(1 - v_{m1}^2/v_{m2}^2)}{1 - v_{m1}^2 f_1^2/v_{m2}^2 f_2^2} \tag{1.13}$$

and the solution for actual LOS velocity v_a takes the form of

$$v_c^2 = \frac{f_2^2 v_{m2}^2 - f_1^2 v_{m1}^2}{f_2^2 - f_1^2}. \tag{1.14}$$

Equation 1.12 - 1.14 provide a computationally simple method for the approximation of both plasma frequency and refractive index based on SuperDARN frequency switched radar data.

These studies provided a correction factor based on years of data which may not be appropriate for all scatter scenarios. A solution based on case studies may prove as a better solution. These studies also tended to use crude range gate selection for which scatter was intended to be examined (e.g., using range gates 20-35 in [*Gillies et al.*, 2011]). Using more analytically rigorous methods to identify the spatial boundaries of scatter may help improve this correction factor.

The most significant point is that these studies were all performed at either high or

polar latitudes, meaning all these SuperDARN radars require a high degree of refraction in order achieve scattering due to the orientation of magnetic field lines. Applying these results to mid-latitude SuperDARN data may not be appropriate due to the significantly different propagation nature. A study at mid-latitudes is required in order to quantify these affects and answer the following question: what is the required correction factor for mid-latitude SuperDARN velocities?

1.6 Objectives

The purpose of this thesis is to explore the refractive effects of the ionosphere at mid-latitudes using SuperDARN radar frequency switched data. The radar for this study is located in Blackstone, Virginia. The significance of understanding the refractive effects of the mid-latitude ionosphere comes from previous studies of the high-latitude ionosphere, which have shown that the plasma convection velocities measured by SuperDARN radars tend to be lower compared to other types of measurements. This effect has been examined in detail at high latitudes and found to be significant but has yet to be explored at mid-latitudes which ultimately brings into question the velocity magnitudes reported by mid-latitude SuperDARN radars. This thesis will present findings to support the claim that LOS velocities observed by mid-latitude SuperDARN radars are effected little by refractive effects and require little to no velocity correction factor.

This thesis uses the spatial variability and more importantly the velocity variability of frequency switched data from the Blackstone SuperDARN radar to validate the following statements:

1. Differences between 1/2 hop and 1 1/2 hop ionospheric scatter are easily observable when examining localization and velocity variability.

2. At mid-latitudes, 1/2 hop ionospheric scatter observed by mid-latitude SuperDARN radars during SAIS events is the result of near straight line propagation to the bottom F-region ionosphere [*de Larquier et al.*, 2013]. Refractive effects from ionospheric propagation affect the velocity measurements little and only minor corrections are indicated (¡ 5%).

3. 1/2 hop ionospheric scatter observed by mid-latitude SuperDARN radars is heavily effected by ionospheric refractive effects. Because of this,

   (a) the localization of a frequency switched pair of LOS velocities is questionable, implying that scatter from before and after a frequency switch may not be occurring at the same region of space.

   (b) the LOS velocity magnitude is strongly effected by the refractive index of the ionosphere for 1 1/2 hop propagation. A velocity correction factor based on the ionospheric refractive index may need to be implemented, though the nature of 1 1/2 hop propagation may make that difficult.

4. Refractive index estimation through frequency switching using SuperDARN radars is possible at mid-latitudes. Refractive index values for 1/2 hop scatter will be close to unity while values for 1 1/2 hop scatter will be less than unity (closer to 20%, similar to values observed at high latitudes).

1.7 Thesis Organization

This thesis begins by describing the methodology used for processing SuperDARN radar velocity data for the purposes of this research. This section progresses from discussion of basic velocity data to derivation of the final product for analysis and gives justifications for

each step. The next section presents a study of some of the frequency, localization, and velocity ambiguities encountered in this research and uses observations to support findings. These findings are then used in the next section to estimate refractive index values in the mid-latitude ionosphere using the Blackstone SuperDARN radar. Lastly, a project is presented on an educational Python radar platform, pyRADAR, geared at High-School aged students in order to broaden exposure to radar and signal processing concepts. This thesis then concludes with future work suggestions.

Chapter 2

Analysis of Refractive Effects on Mid-Latitude SuperDARN Velocity Measurements

2.1 Introduction

Previous studies have found that high latitude SuperDARN plasma convection velocity estimates have been routinely underestimated due to the assumption of a unity refractive index. A correction factor for these velocities is required in order to more accurately reflect other measurements, and several studies have proposed techniques for determining this correction factor. One such technique proposed in *Gillies et al.* [2011] uses frequency switching between azimuthal scans to estimate the refractive effects on measured velocities. These studies provided a correction factor based on many years worth of data and were all performed at high latitudes. This effect has yet to be explored at mid-latitudes. To determine this effect, a case study driven analysis has been performed to more accurately determine correction factors required for mid latitude plasma convection velocities.

This research concerns itself with frequency-switched velocity measurements taken from the Blackstone SuperDARN radar. Six prime events for both ½ hop and 1½ hop ionospheric scatter are used and the dates are tabulated in Table 2.1. The conditions for the ½ hop ionospheric tended to be quiet, with Dst Index values never becoming lower than -10 nT.

Table 2.1: Dates for events used in this research.

1/2 Hop Scatter	**1 1/2 Hop Scatter**
12/15/2013	3/3/2014
1/14/2014	3/21/2014
2/11/2014	4/7/2014
2/13/2014	4/10/2014
2/14/2014	4/17/2014
3/17/2014	4/20/2014

This scatter type can be classified as SAIS and tends to have low westward velocities (i.e., on the order of -30 m/s). The conditions for the 1 1/2 hop ionospheric tended to be slightly more active, with Dst Index values usually between -10 and -20 nT. This scatter is most likely auroral and usually has both westward and eastward velocities, sometimes exceeding 500 m/s in magnitude. The time span considered in each event is usually between 5-7 hours in length and the total number of frequency switched pairs per event is usually around a few thousand. Data has been processed and smooth to remove the stochastic nature of the data. More can be found in Appendix A.

The structure of research has been divided into three sections:

1. Examine the spatial distribution of mid latitude frequency switched ionospheric scatter data for signs of refractive effects. Compare the 1/2 hop and 1 1/2 hop ionospheric scatter modes and determine if a discernible difference exists.

2. Quantify the background variability of velocity data in order to better compare frequency switched velocities.

3. Calculate refractive indices based on two approaches and contrast those results to previous works.

The summation of this work will provide evidence that night time 1/2 hop ionospheric scatter

experiences little to no measurable refraction when examining frequency switched velocities. This result implies that little to no correction factor is required for this velocities, meaning that those estimated LOS velocities v_m previously reported by mid-latitude SuperDARN radars are most likely representative the actual LOS plasma convection velocities v_c.

2.2 Localization Differences in Mid-Latitude SuperDARN Ionospheric Scatter

At HF band frequencies the ionosphere acts as a dispersive media, much like light propagating through glass. Different frequencies will experience different degrees of refraction, meaning they will propagate at different velocities according to Equation 1.7. This change in velocity could possibly impact the geospatial distribution of ionospheric scatter when using a frequency switched mode, causing scatter to come from different regions of space. This spatial difference will be defined as localization difference. Localization difference observations are presented in this section for mid latitude SuperDARN ionospheric scatter by first quantifying the stability of the frequencies used.

2.2.1 Frequency Variability

The velocities examined in this research are from a frequency switched mode, meaning sequential azimuthal scans are at alternate frequencies. In an idealized system the frequency before and after a frequency switch would always be the same. However in a real world system the noise power spectrum is turbulent and must be accounted for. SuperDARN radars typically compensate for this variable noise power spectrum by performing a "clear frequency search" which ultimately creates two distributions of frequencies centered around two nominal frequencies.

Before a dwell is made in a beam direction in a SuperDARN system, an optimization routine is done in order to find the bandwidth with the lowest noise power. A target center frequency is suggested and the routine examines a total bandwidth of 300 kHz around this frequency. A typical SuperDARN transmission bandwidth is 40 kHz, so the routine typically attempts to find the lowest noise power for a 40 kHz bandwidth, though this bandwidth depends on the current mode the radar is running. This routine is performed in order to increase the SNR of radar echoes but has an interesting effect on frequency switched modes. Figure 2.1 (top) presents frequency statistics for beam 12 on 2/11/2014 from 4:00 UTC to 12:00 UTC using the Blackstone SuperDARN radar while it ran a frequency switched mode. Ionospheric activity was low during this period. Note the two distinct distributions with an approximate bandwidth of 300 kHz. It can be observed that the higher frequency content is more variable than the lower frequency content. From Figure 2.1, it is possible that the frequency difference between the two distributions may be as low as 350 kHz or as high as 850 kHz. This is a nontrivial difference and will have propagation ambiguity implications. Figure 2.1 (bottom) expands on this by including all beams from the same event and shows that the distributions for all beams have a similar trend, which illustrates how prevalent the frequency variability is.

It should be observed that the routine never causes the distributions to overlap. This implies that the general trend of switching between two independent frequencies is maintained and observations may be grouped into lower frequency observations f_{low} and into higher frequency observations f_{high}. Care in considering the frequency separation for a switched event should be taken as fluctuations will impact localization results. The frequency separation before and after a frequency switch is examined in Figure 2.2 for the same period and for all beams. The light-green highlighted area represents approximately 99% of the distribution, meaning that 99% of the time the separation is between 400 kHz and 850 kHz for this 1/2

hop event. Examining the distribution more closely shows that it favors higher frequency separation with a mean of approximately 650 kHz and approximately 90% of the distribution falling between 500 kHz and 800 kHz. This examination shows that while the variability is still nontrivial, it is not as severe as first speculated. However, care must still be taken when examining frequency switched observations as this variability in frequency separation may affect localization and velocity difference properties between frequencies.

Another way to approach this problem is by examining the statistics of the ratio of the lower frequency (before the switch) and the higher frequency (after the switch) f_{low}/f_{high}. This ratio and it's variability are important as they are a key factor in Equation 1.13. If the standard deviation is high, it will need to be accounted for. Results are presented for the same event as previous in Figure 2.2. The distribution in Figure 2.3 appears to have bounds at 0.925 and 0.965, though 95% of the distribution is approximately between 0.925 and 0.96. This is a change of approximately 3.7%, and should not place a significant bias on the data. It should be noted that these results are for quiet-time ½ hop ionospheric scatter events. For a auroral event presenting 1½ hop scatter, things tend to appear differently. Similar results are presented below for an event on 4/17/2014 from 3:00 UT to 8:00 UT. The top plot in Figure 2.4 shows that for auroral scatter the routine has a bias towards individual frequencies. This is most likely due to dominant sources of noise appearing in the high latitude ionosphere. The bottom plot in Figure 2.4 demonstrates that during auroral scatter the frequency spread seems to be relatively bimodal, choosing tight frequency bands rather than the wide distribution exhibited by the ½ event.

2.2.2 IRI Model Raytracing

It was discussed previous in Chapter 1.3 that refraction of electromagnetic waves behaves according to Snell's Law, which states that for some electromagnetic wave at a boundary

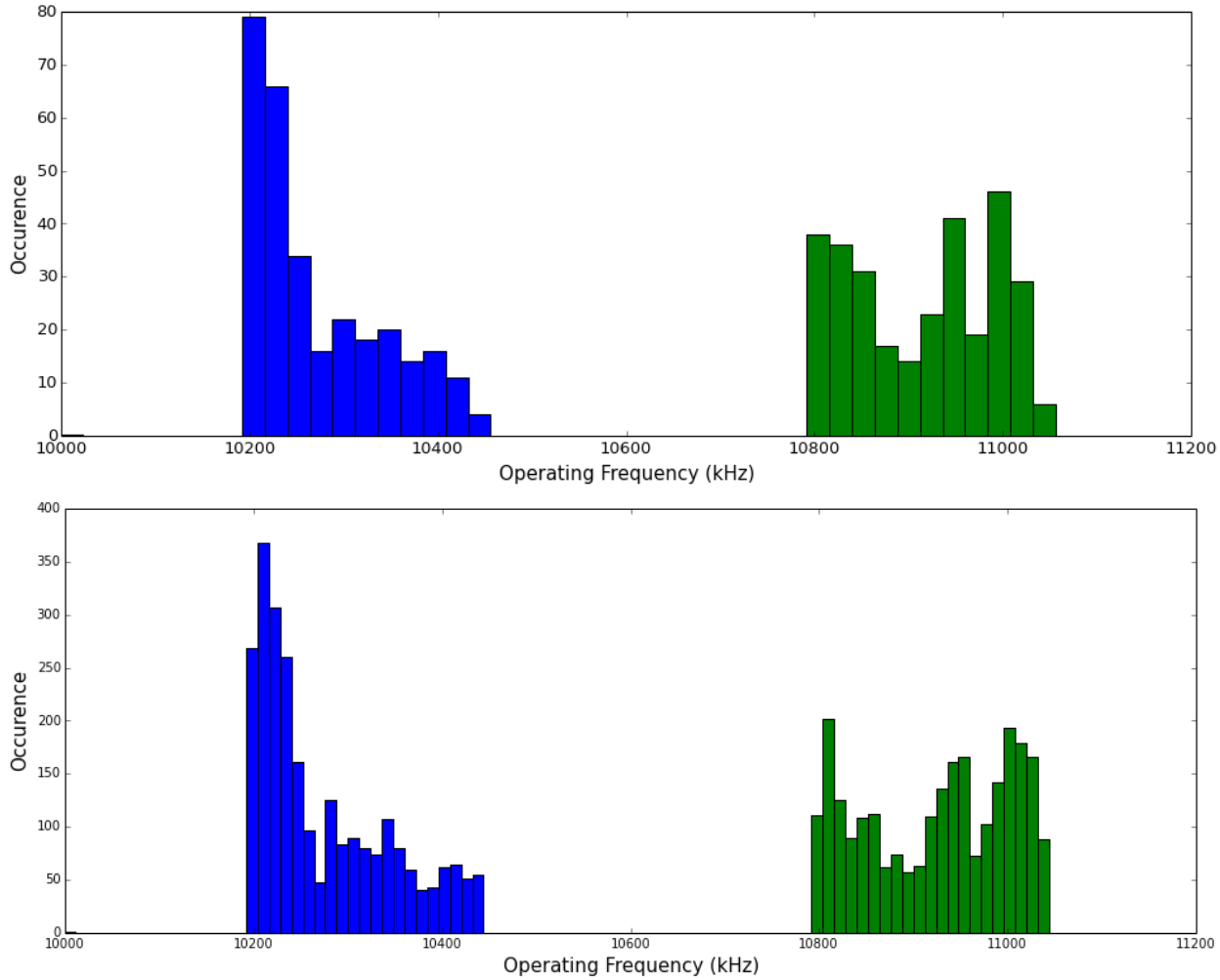

Figure 2.1: Variability of the radar frequency from dwell to dwell for an event on 2/11/2014. Presented is the frequency statistics using a single beam, specifically beam 18, (top) and all beams (bottom). Two distributions colored green and blue can be observed due to the use of a frequency-switched mode.

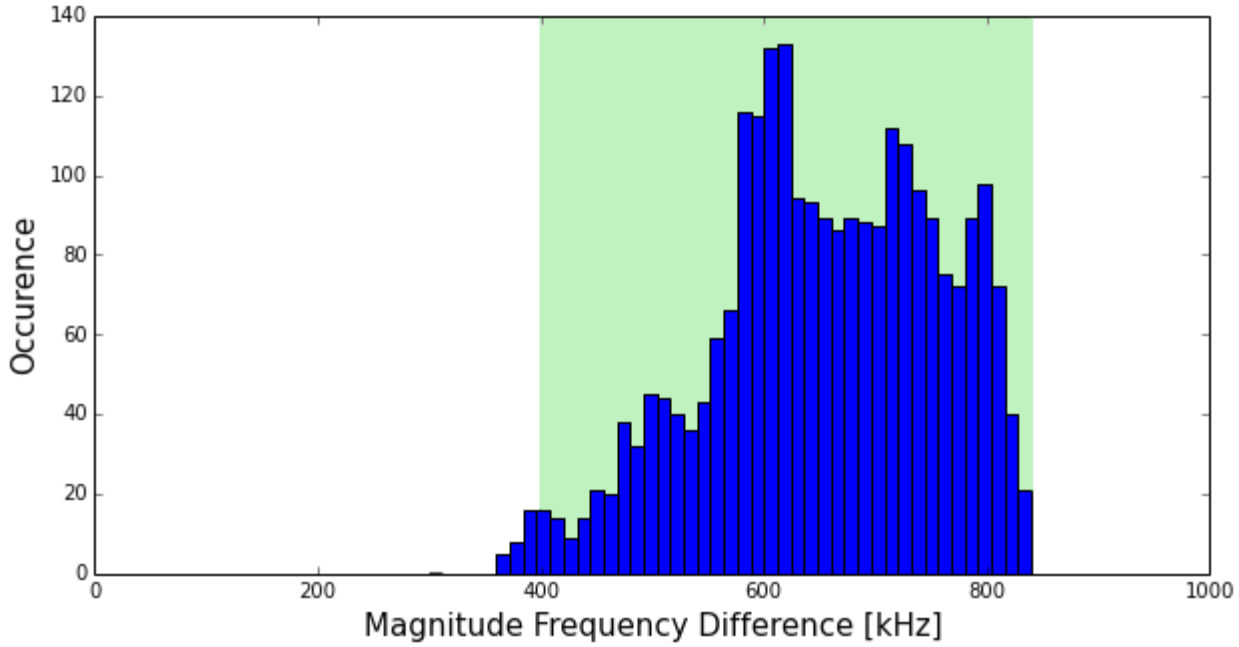

Figure 2.2: Statistics for frequency difference for a typical ½ hop event using a frequency switched mode. The green shaded area represents 99% of the distribution. High frequency separation appears to be more common than lower frequency separation.

between two media, the degree of refraction will be proportional to the ratio of the refractive indices of the two media as written in Equation 1.5. Despite the ionosphere being a medium with a continuum of electron density gradients, the fundamentals of Snell's Law still apply meaning a ray oblique to the ionosphere will ultimately refract back toward the earth given that the wave frequency is greater than the plasma frequency and the angle of incidence is less than the critical angle, or the greatest angle of incidence at which a ray may return back to the Earth. An approximation of the refractive effects through the ionosphere can be done via ray-tracing, which solves for the wave trajectory with incremental application of Snell's Law using an effective localized refractive index. Without a refracting media to encounter, rays would simply propagate outward radially as shown in Figure 2.6. Luckily the ionosphere is not an isotropic medium and gradients in plasma density will allow for refraction. This technique will be used in this section to examine localization differences

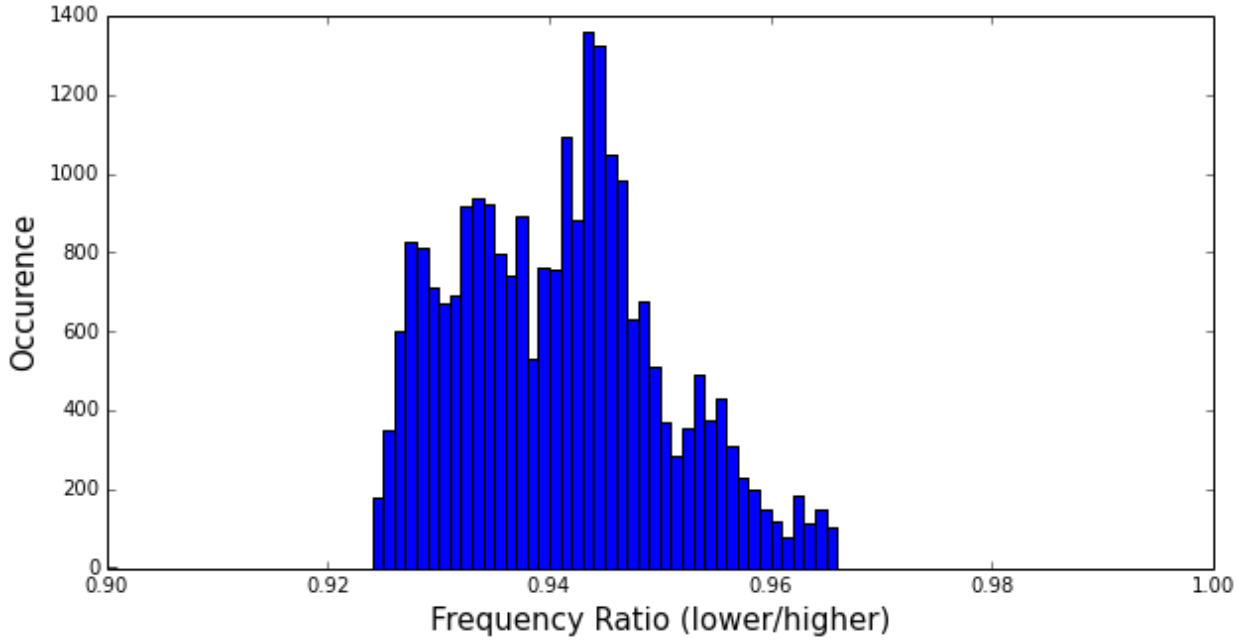

Figure 2.3: Statistics for ratio of the lower frequency to the higher frequency f_{low}/f_{high}. The plot clearly shows a low degree of variability, meaning that the variations in distance for frequency switches is relatively negligible.

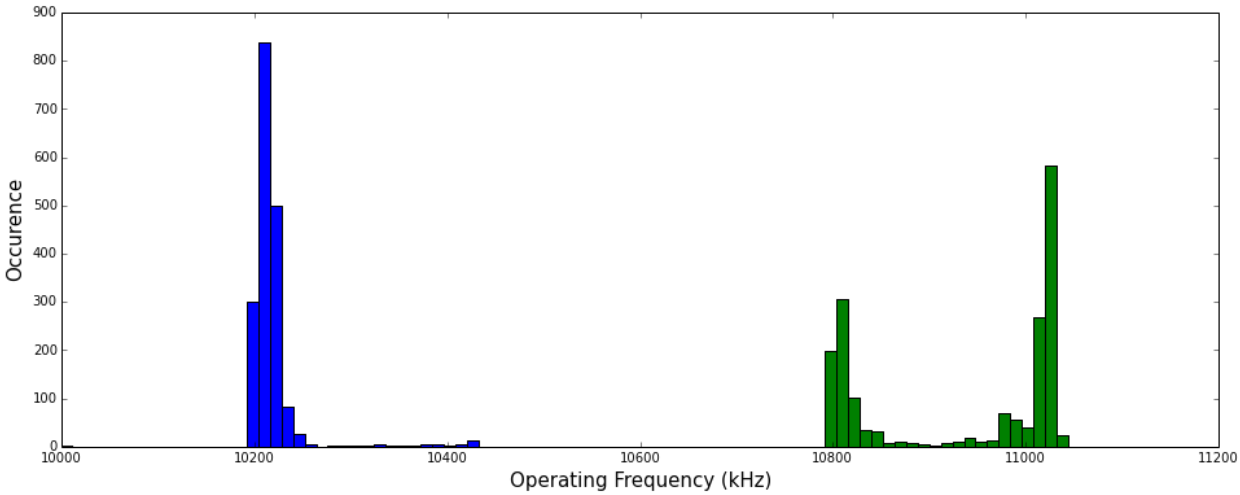

Figure 2.4: Statistics for frequency variability for a typical auroral event exhibiting 1½ hop scatter using a frequency switched mode. Note the differences between this and Figure 2.1, especially how frequency selective the system becomes.

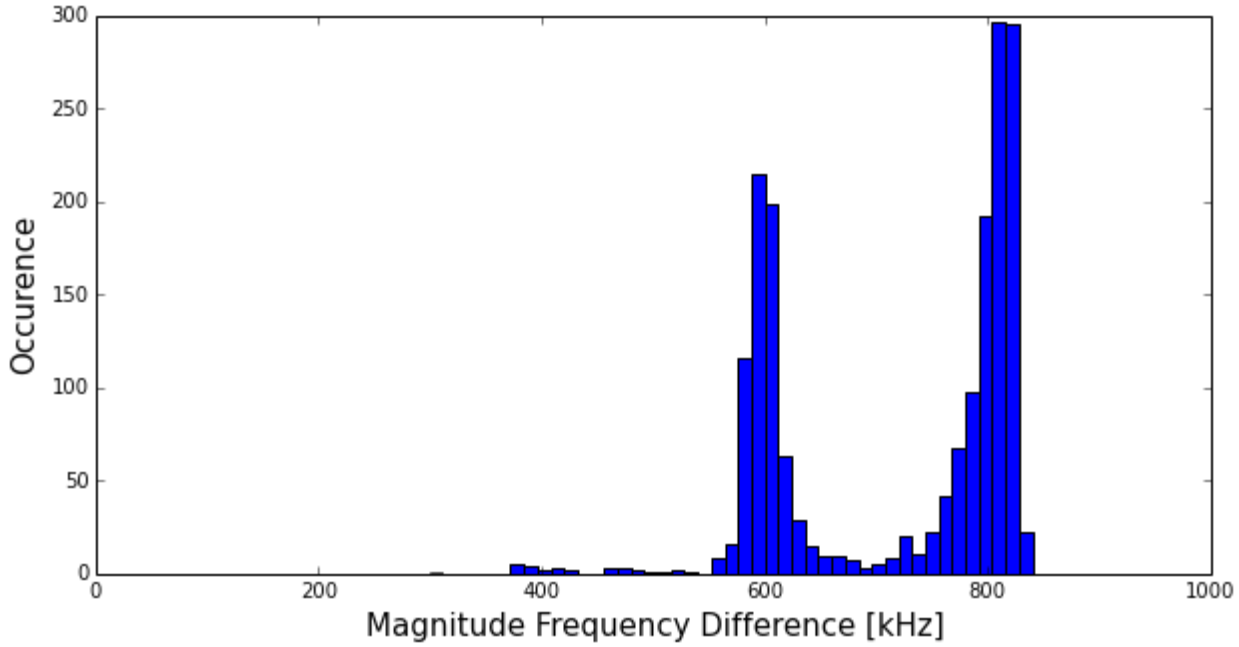

Figure 2.5: Statistics for frequency variability for a typical auroral event exhibiting 1½ hop scatter using a frequency switched mode. Note how modal the system has become when compared to Figure 2.2.

in different ionospheric propagation modes (specifically ½ hop and 1½ hop ionospheric scatter).

Two rays at slightly different frequencies (10.2 MHz and 10.9 MHz) are shown in Figure 2.7 as they propagate through a populated model IRI ionosphere near Blackstone, Virginia on a typical quiet night. The rays are travelling northwestward. The image contains both ½ hop and 1 ½ hop ionospheric scatter, as well as ground scatter content. The ½ hop ionospheric scatter seems to exhibit little localization difference between frequencies (on the order of 10 km), whereas the 1 ½ hop scatter ionospheric scatter exhibits a large localization difference (on the order of 100 km). Because the typical range resolution for a SuperDARN radar is 45 km, this would mean that the scatter observed at two different frequencies are offset by 2-3 range gates. This difference is large enough to make the assumption that the 1 ½ hop scatter from the same launch angle at different frequencies may not be returning

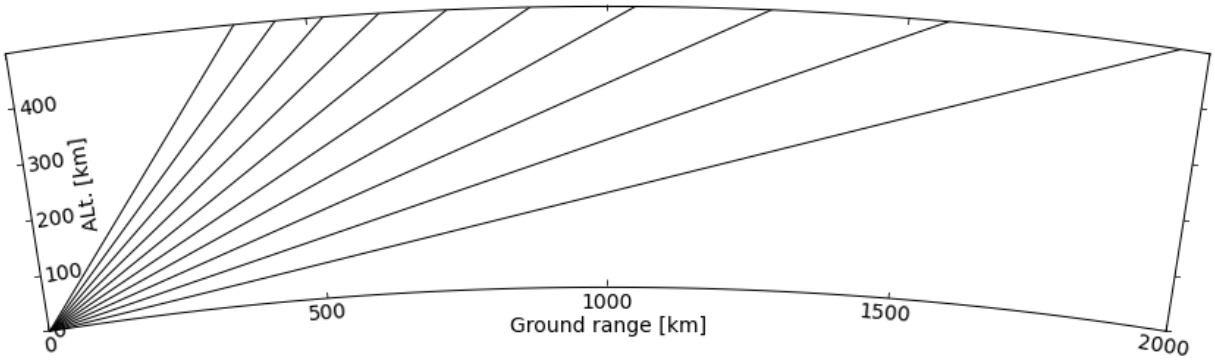

Figure 2.6: Ray-tracing for rays at various launch angles in an unpopulated ionosphere. Due to the nature of freespace propagation, waves will not refractive or reflect meaning that a time delay for rays at different launch angles yields identical slant ranges.

from the same magnetic field lines and are thus not measuring the same volume of space.

A second observation can be made regarding the propagation of the ½ hop ionospheric scatter. From the ray-tracing, it appears that the ½ hop scatter undergoes very little refraction in order to achieve near-perpendicularity with the magnetic field orientation. This implies that the quiet-time LOS velocities observed for ½ hop ionospheric scatter are affected little by refractive affects at mid-latitudes. This hypothesis will be explored in future sections.

2.2.3 Localization Difference Observations

Scenarios for both ½ hop and 1½ hop ionospheric scatter have been compared for localization differences at mid-latitudes using the Blackstone SuperDARN radar. The blob detection algorithm discussed previously allowed for the comparison of a blob's mean range gate position before and after a frequency switch. The localization difference for ½ hop ionospheric scatter is presented in Figure 2.8 while the localization difference for the 1 ½ hop ionospheric scatter is presented in Figure 2.9 and both are the aggregation of 6 individual events listed in Table 2.1. Examining both plots shows that their behaviour matches that predicted by the IRI ray-tracing simulation. Namely, the ½ hop ionospheric scatter exhibits

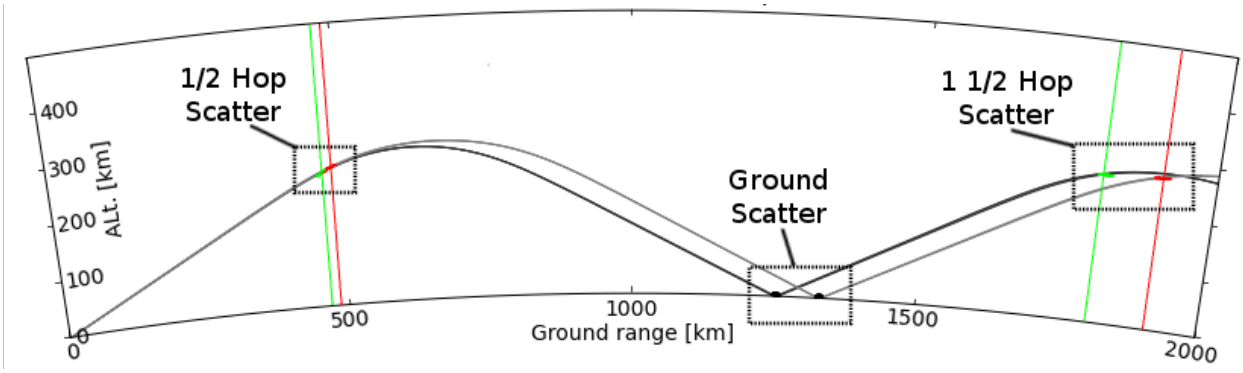

Figure 2.7: Ray-tracing through a populated model IRI ionosphere at two different frequencies. The black ray (10.2 MHz) and the gray ray (10.9 MHz) are launched from the same angle. Green indicates near-perpendicularity for the black ray and red indicates near-perpendicularity for the gray ray. Lines have been added to highlight scatter locations. Significant spreading occurs for the 1 ½ hop ionospheric scatter relative to the ½ hop ionospheric scatter.

little to no range gate offset while the 1 ½ hop ionospheric scatter exhibits an offset of around 2 range gates, favoring the higher frequency content. This observation proves that most scatter from ½ hop ionospheric scatter is likely straight line propagation and is coming from the same region of space implying that LOS velocity measurements before and after a frequency switch are co-located. Conversely, the 1½ hop ionospheric scatter may not be originating from the same region of space, meaning it may not be scattering off of the same magnetic field line. This implies that it may not be valid to compare LOS velocity measurements before and after a frequency switch for the 1½ hop scatter without taking into account range variations in velocity.

2.2.4 Summary

This section has examined the localization differences of backscatter obtained at two different radar operating frequencies. These examinations were done comparing two specific ionospheric scatter scenarios: ½ hop scatter and 1½ hop scatter. The results from this section have shown that due to the near straight line propagation of ½ hop scatter, refraction

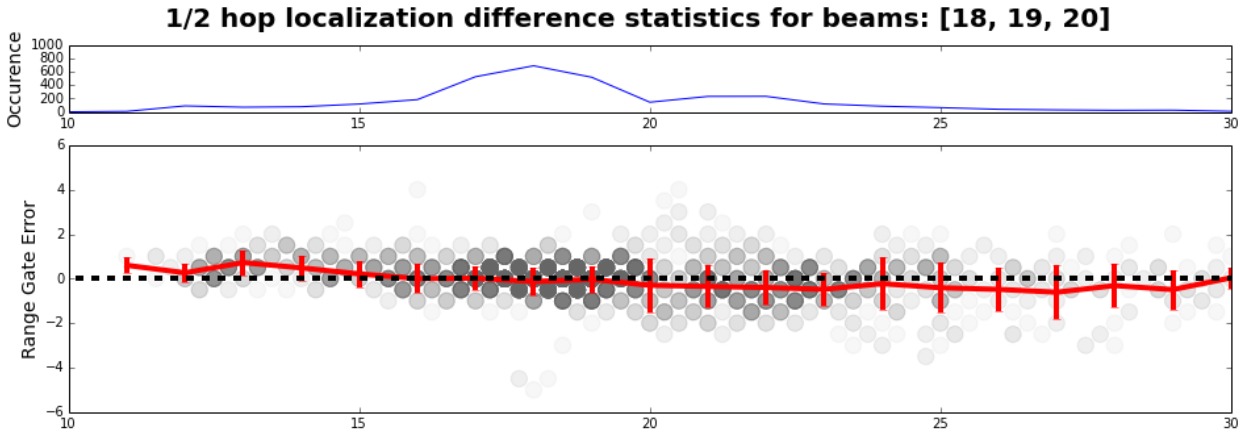

Figure 2.8: Statistics for the 1/2 hop ionospheric scatter scenarios. The top plot illustrates the occurrence of scatter while the bottom plot compares the range gate offset to the mean position in range gates. The 1/2 hop scatter tends to exhibit little to no range gate offset. Range gate offset is calculated by subtracting the range of the high frequency content from that of the low frequency content.

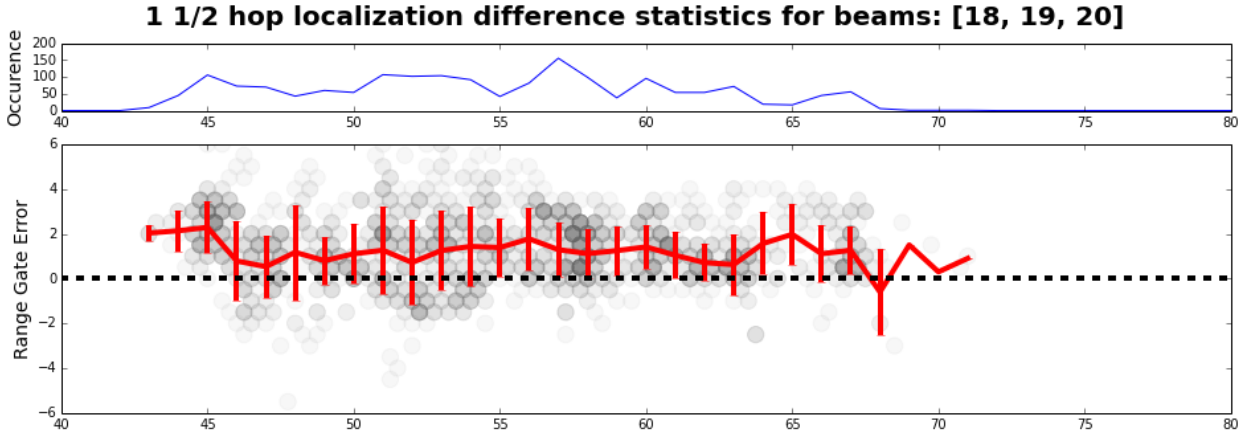

Figure 2.9: Statistics for the 1 1/2 hop ionospheric scatter scenarios. The top plot illustrates the occurrence of scatter while the bottom plot compares the range gate offset to the mean position in range gates. The 1 1/2 hop scatter tends to exhibit a range gate offset toward the high-frequency content. Range gate offset is calculated by subtracting the high frequency content by the low frequency content.

is low, meaning non-localization effects are small. Conversely, 1 ½ hop scatter tends to suffer from significant non-localization and is highly frequency dependant. Frequency dependant refraction may not be the only contributing factor to localization difference (e.g. uneven earth scatter surface, changes in return path, and plasma gradient variability) but this work seems to indicate that it is the principle component. With this finding in mind, the subsequent velocity comparisons that will be presented are then assumed to be much more valid for ½ hop scatter. Using this, in the next section we will exploit velocity variability in quiet-time events to estimate refractive index values in the mid-latitude ionosphere.

2.3 Velocity Variability Investigation

It was stated previously in Section 1.3 that when a SuperDARN radar signal refracts through the ionosphere the wave group velocity slows. This should have an effect on the LOS velocity measurements made by SuperDARN radars as it causes the measured LOS velocity to be slower than the actual LOS $\mathbf{E} \times \mathbf{B}$ plasma drift velocity. This is a significant problem in high-latitude systems but it has yet to be studied at lower latitudes. This section explores velocity variability in ½ hop scatter by first looking at the time correlation for closely spaced same frequency scans.

If a range bin is populated before a frequency switch occurs and is still populated after it has returned to the original frequency (i.e., a range bin populated at t and t + 2Δt), those velocity values may be compared. This comparison gauges how variable velocity measurements are on a dwell-to-dwell basis. This section presents results for two events, one sub-auroral ½ hop scatter scenario (2/11/2014) and one auroral 1½ hop scatter scenario (4/17/2014). These results are presented in Figure 2.10 for the ½ hop scatter scenario and in Figure 2.11 for the 1 ½ hop scatter scenario. In each case, the right plot shows the histogram of velocity changes for that event and the left plot shows the actual distribution

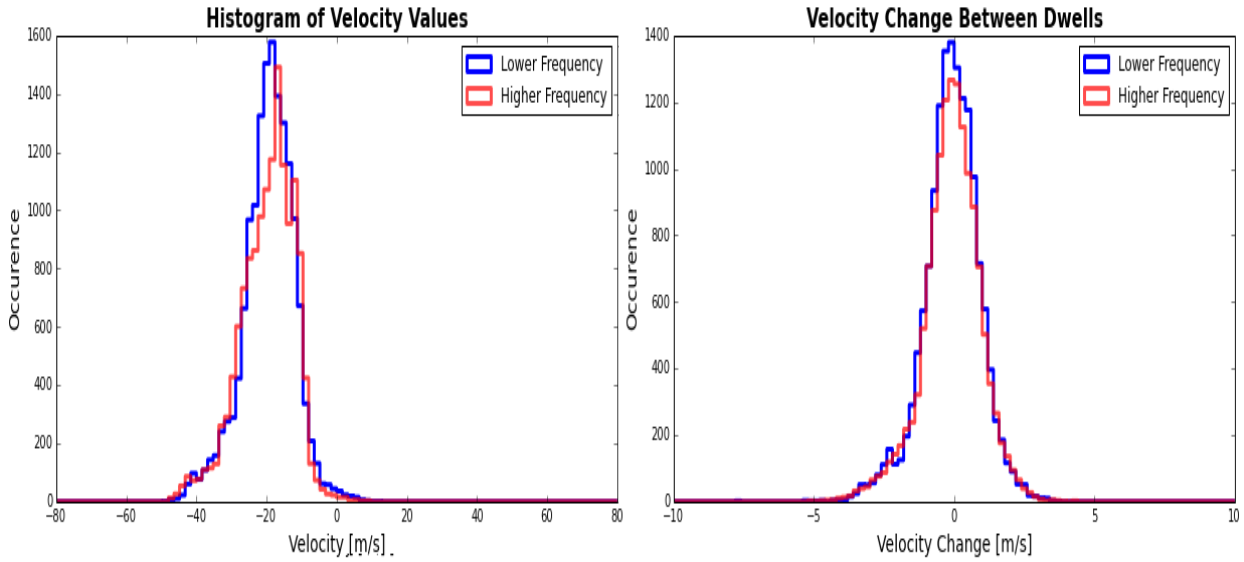

Figure 2.10: Dwell-to-dwell velocity variability statistics for a quiet-time 1/2 hop scatter scenario (2/11/2014). The left plot illustrates the actual velocity distribution v while the right plot illustrates the magnitude change in velocity δv. Both distrbutions appear very similar. Variability is examined and tabulated in Table 2.2.

of velocities. At first glance, it is obvious that the magnitude of change for the 1/2 hop scatter scenario is much less than that of the 1 1/2 hop scatter scenario. However, the goal of this section is to measure statistical variability and not magnitude of change, meaning a more valid comparison would be the ratio of the standard deviation $\sigma_{\delta v}$ of the magnitude velocity difference to the mean of the actual velocity distribution μ_v or

$$Variability = \left| \frac{\sigma_{\delta v}}{\mu_v} \right|. \tag{2.1}$$

This ratio allows for a more accurate comparison of variability than simply examining the magnitudes of the changes. A variability of 1 would mean that $\sigma_v = \mu_v$. These results are tabulated in Table 2.2 for mean of the velocity distribution μ_v, the standard deviation of the velocity change $\sigma_{\delta v}$, and the mean of the velocity change $\mu_{\delta v}$, as well as the variability.

In total, the results from Figure 2.10, Figure 2.11, and Table 2.2 show that the 1/2 hop

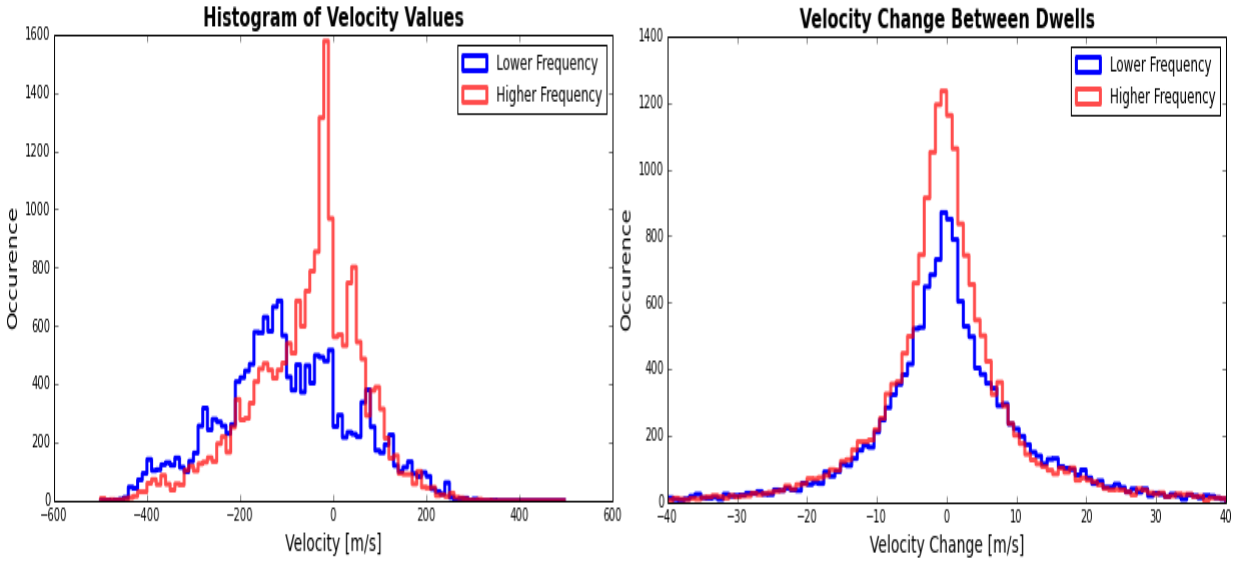

Figure 2.11: Dwell-to-dwell velocity variability statistics for a auroral 1½ hop scatter scenario (4/17/2014). The higher frequency distribution seems to have a larger number of data points, most likely indicating the propagation conditions for the auroral event favored a higher frequency. Variability is examined and tabulated in Table 2.2.

Table 2.2: Variability of Velocity (dwell-to-dwell)

	Type	**Low Frequency**	**High Frequency**
½ hop	μ_v	-19.5 m/s	-21.1 m/s
	$\mu_{\delta v}$	-0.08 m/s	-0.09 m/s
	$\sigma_{\delta v}$	1.04 m/s	1.03 m/s
	Variability	0.05	0.05
1 ½ hop	μ_v	-80.2 m/s	-45.3m/s
	$\mu_{\delta v}$	0.88 m/s	0.44 m/s
	$\sigma_{\delta v}$	11.8 m/s	11.1 m/s
	Variability	0.15	0.25

scatter scenario exhibits a lower degree of variability from dwell-to-dwell than the auroral 1 1/2 hop scatter scenario for both the lower and higher frequency. This outcome indicates that on a 2 minute time resolution-scale, 1/2 hop velocity values are more stable than auroral 1 1/2 hop velocity values. This outcome is expected, since the 1 1/2 hop scenarios generally occur in the more dynamic auroral region and have a much more refraction dependant propagation mode. Another significant result is the nearly zero mean associated with the dwell-to-dwell variability of velocity values $\mu_{\delta v}$ in Figure 2.10 and Figure 2.11. This indicates that the background velocity variability has no general positive or negative trend and is relatively Gaussian. This background variability is most likely due to the statistical nature of the scattering source, though some may come from sky noise. The statistical nature of the scattering source is result of the volume scattering souce having multiple scattering structures, each with their own velocity contributions and life times [*Ponomarenko et al.*, 2012]. The standard deviation of this distribution gives insight into how background variability will effect frequency switched velocity pairs, and also allows for intelligent removal of low velocity values due to the background variability. This will be explored in the next section.

These results allow for a better understanding of the background variability of the frequency velocity data. If velocities are relatively stable on a 2 minute time-scale, then velocities on a 1 minute time-scale should also be stable. This implies that variability of frequency switched velocities is more of a product of actual refractive effects than system variability. With this quantified, a more accurate measurement of frequency switched velocity variability can me made allowing for a more accurate estimation of refractive index.

2.4 Refractive Index Estimation at Mid-Latitudes

This section presents refractive index estimation results, and consequently velocity correction factor results, using the Blackstone SuperDARN radar. First, frequency switched ve-

locity measurements are compared in order to discern a trend of magnitude change between frequencies. These results are then expanded upon to actual refractive index estimation using two approaches. Lastly, a storm time 1/2 hop ionospheric case study is presented.

2.4.1 Switched Velocity Statistics

The change in velocity due to the frequency dependant nature of the ionosphere is crucial for estimating refractive index values in frequency switched SuperDARN velocity data. Examination of Equation 1.11 shows that for identical velocities, a decrease in refractive index n_s will yield a decrease in the magnitude of LOS velocity measurements v_s. Examination of Equation 1.10 yields that for identical plasma frequencies f_p, an increase in radar operating frequency f will increase the observed refractive index n_s. From this, a frequency switch from a lower frequency to a higher frequency will always result in higher SuperDARN LOS velocities. This only holds in a noiseless, time invariant system. Due to the stochasticity of SuperDARN radar measurements, this LOS velocity difference must be found statistically as the variability of the data may hide the actually trend on a dwell-to-dwell basis. If this can be observed, it will validate the approach of using frequency switching in SuperDARN radars at mid-latitudes to estimate refractive index values. Examples are presented for both a 1/2 hop scatter scenario and a 1 1/2 hop scatter scenario. Velocity values are compared by subtracting the magnitude of the lower velocity from the magnitude of the higher velocity $\delta v = |v_{low}| - |v_{high}|$. Situations may occur for which a frequency switched velocity pair may have opposite signs. In this scenario, the value of δv will not represent the desired magnitude difference and will create artificially lower values (e.g., v_{low} = 10 m/s and v_{high} = -8 m/s has a magnitude difference δv = -2 m/s). In order to compensate for this, velocity values that were close to zero where thrown out from the final dataset. Results of this process are presented in Figure 2.12 (left) and Figure 2.12 (right) for a 1/2 hop scatter scenario and a 1

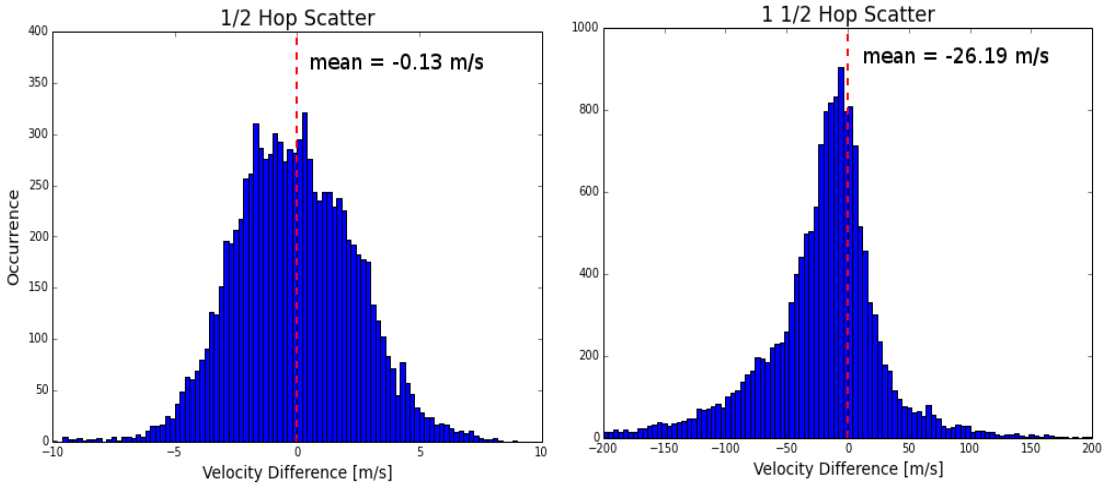

Figure 2.12: LOS velocity difference δv statistics for a 1/2 hop scatter scenario and a 1 1/2 hop scatter scenario respectively. The 1/2 hop scatter comes from 2/11/2014 and the 1 1/2 hop scatter comes from 4/17/2014. Both include all beams and were measured using the Blackstone SuperDARN radar. Velocity values are determined by subtracting the velocity magnitude of the lower frequency content by the magnitude of the higher frequency content. The mean of the distribution for the 1/2 hop scatter was -0.13 m/s and the mean of the distribution for the 1 1/2 hop scatter was -26.19 m/s.

1/2 hop scatter scenario respectively. The vertical dashed red line represents zero variability.

As expected, both plots in Figure 2.12 show the general trend of an increase in velocity magnitude when a frequency shift is performed from lower frequency to a higher frequency; however, the mean in the 1/2 hop scatter scenario is very close to zero. This would indicate that the degree of refraction is relatively low. This supports the assumption that quiet-time 1/2 hop ionospheric scatter is nearly straight line propagation at mid-latitudes. Because of this, the 1/2 hop scatter does not exhibit a strong trend in velocity difference. Conversely, the 1 1/2 hop scatter should experience a great deal of refraction, the distribution reflects this assumption, showing a strong statistical decrease in LOS velocity measurements when frequency increases. This analysis has been applied to several different event periods, specifically those tabulated in Table 2.1, for both 1/2 hop and 1 1/2 hop scatter scenarios, and the means of those distributions a tabulated in Table 2.3.

Table 2.3: Tabulation of Mean Velocity Difference $\mu_{\delta v}$ for 1/2 hop and 1 1/2 hop scatter scenarios

Date	**1/2 Hop Scatter**	**1 1/2 Hop Scatter**	$\mu_{\delta v}$	A-Index (Planetary)
12/15/2013	X		-0.31 m/s	5
1/14/2014	X		-0.09 m/s	8
2/11/2014	X		-0.13 m/s	3
2/13/2014	X		-0.05 m/s	2
2/14/2014	X		-0.16 m/s	4
3/17/2014	X		-0.06 m/s	2
3/3/2014		X	-19.13 m/s	3
3/21/2014		X	-17.42 m/s	10
4/7/2014		X	-16.83 m/s	5
4/10/2014		X	-12.69 m/s	15
4/17/2014		X	-26.19 m/s	11
4/20/2014		X	-70.94 m/s	20

The results tabulated in Table 2.3 show clearly that there exists some bias when switching from a lower frequency to a higher frequency, though it is much less present in all of the 1/2 hop scatter scenarios. This is most likely due to the stochastic nature of the scatter causing any actual offset to be masked and may create scenarios where the mean is actually positive. On the other hand, the 1 1/2 hop scatter scenarios all exhibit strong frequency dependence, proving that the velocity values measured will on average decrease when performing a frequency switch. Once again, this result is somewhat as expected since the 1 1/2 hop scatter experiences more refraction due to the nature of its long range propagation. The more an ionospheric propagating wave is affected by refraction, the more the LOS velocity information is susceptible to underestimations. These results give justification for estimating refractive index due to the expected negative velocity difference observed.

2.4.2 Refractive Index Statistics

Due to the possibility of underestimation in plasma convection velocities observed by SuperDARN radars, a correction factor may be needed to more accurately reflect other measurements. Measuring the refractive index of the scattering volume would give this correction factor. The scattering volume's plasma frequency will be estimated using the approach described in Section 1.5, specifically using Equation 1.13, but two different approaches will be used to calculate refractive index. The two approaches are named the "mean of ratios" approach (MoR for short) and the "ratio of means" approach (RoM for short). These two approaches can be described as follows:

1. Mean or Ratios (MoR) approach
   (a) Produce a distribution of frequency-switched velocity ratios.
   (b) Create a distribution plasma frequencies, which will intern become a distribution of refractive indices.
   (c) Calculate mean refractive index.
2. Ratio of Means (RoM) approach
   (a) Produce distributions for lower and higher frequency velocity content.
   (b) Calculate mean of the two distributions. Calculate a single plasma frequency from these two means and the two average radar frequencies.
   (c) Calculate mean refractive index.

A more descriptive explanation of the MoR technique is to use all velocity switched values to determine a time series of plasma frequency values for the time span in question. The mean of this distribution is used as the representative refractive index, thus the name

"mean of ratios" as the result is based off the mean of all the velocity switched values. An example of this is presented in Figure 2.13 for a 1/2 hop and a 1 1/2 scatter event. One disadvantage of this approach is it has the problem of including non-physical solutions to Equation 1.10. Namely, a refractive index greater than unity requires an imaginary plasma frequency, which should not exist. Nevertheless, these values are included in this approach as it is assumed they are real but represent the fluctuating nature of the scatter and removing them would skew the actual measured refractive index. However, plasma frequency f_p values greater than radar operating frequency f are not included in the final data set as they create imaginary refractive indices.

A more descriptive explanation of the RoM is that it relies on the average velocity values for the determination of refractive index. An average starting velocity v_{start} was first determined and a second velocity v_{end} was determined by adding the first velocity value to the average velocity difference $\mu_{\delta v}$. These two velocity values can then be used with average values for f_{low} and f_{high} in Equation 1.13 to determine an average plasma frequency for this event, which can in turn be used in Equation 1.10 to determine an average refractive index for the event, thus the name "ratio of means" is it compares the ratio of the mean velocity values. This approach yields a more analytically rigorous approach but requires a long time series to produce an accurate values and is susceptible to irregular data trends.

Essentially, the difference between the two techniques lies in when the mean refractive index is determined: the MoR approach determines the mean refractive index from the distribution of frequency switched velocities while the RoM approach determines the mean refractive index from the distribution of velocities and the mean switched velocity magnitude. Both of these approaches are used to evaluate entire 1/2 hop scatter events in order to determine refractive index values.

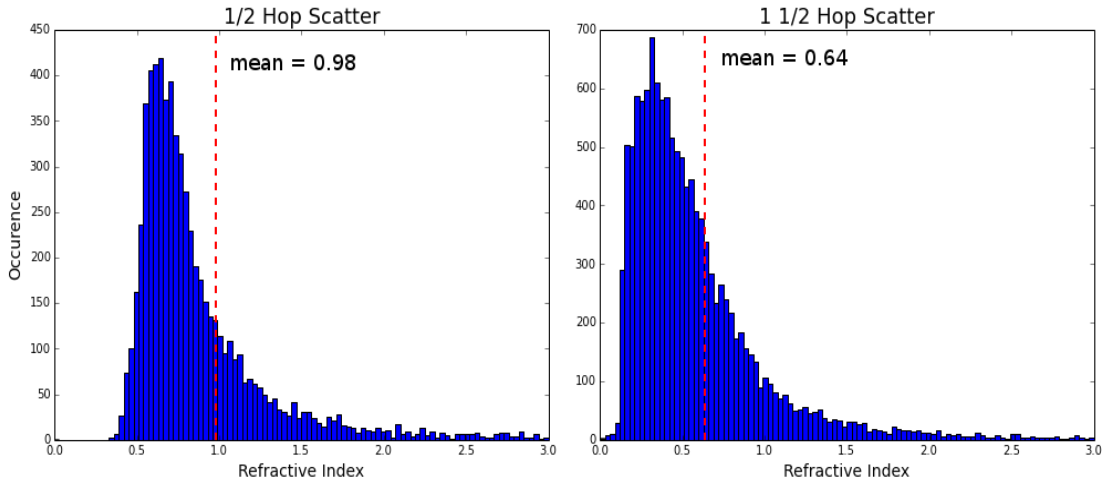

Figure 2.13: Refractive index statistics for a 1/2 hop scatter scenario and a 1 1/2 hop scatter scenario respectively. The 1/2 hop scatter comes from 2/11/2014 and the 1 1/2 hop scatter comes from 4/17/2014. Both include all beams and were measured using the Blackstone SuperDARN radar. Refractive index values were calculated using Equation 1.10 and Equation 1.13. The mean of the distribution for the 1/2 hop scatter was 0.98 and the mean of the distribution for the 1 1/2 hop scatter was 0.64.

The results in Figure 2.13 show that the 1/2 hop scatter appears to have a refractive index very close to unity (i.e., $n \sim 0.98$). Again, this is consistent with the previous finding that the quiet-time mid-latitude ionospheric scatter corresponds to very little refraction and is most likely obtained via near straight line propagation to the bottom-side F-region ionosphere. Conversely, the 1 1/2 hop scatter appears to have a refractive index less than one (i.e., $n \sim 0.64$), indicating a high degree of refraction. This reflects the velocity comparison study done in the previous section and lends further validity to the concern that refraction corrupts the measured velocity values. However, the validity of the actual refractive index value is questionable though, as 1 1/2 hop scatter propagation causes localization issues as found previous in Section 2.2.3. Refractive index values for several additional 1/2 hop scatter events are presented in Table 2.4. The tabulated tabulated reflect those in plotted in Figure 2.13. Most refractive index values for the 1/2 hop scatter scenarios tend to be near unity and both refractive index values obtained using the RoM approach and MoR approach agree

Table 2.4: Tabulation of Mean Refractive Index for 1/2 hop scatter scenarios containing mean velocity μ_v, variability of velocity difference $\sigma_{\delta v}$, mean velocity difference $\mu_{\delta v}$, and the average refractive index n_1 for the MoR approach and n_2 for the RoM approach

Event Date	μ_v	$\sigma_{\delta v}$	$\mu_{\delta v}$	n_1	n_2
12/15/2013	-21.1 m/s	0.77 m/s	-0.31 m/s	0.91	0.93
1/14/2014	-25.2 m/s	0.59 m/s	-0.09 m/s	0.99	0.97
2/11/2014	-22.4 m/s	0.74 m/s	-0.13 m/s	0.98	0.96
2/13/2014	-37.3 m/s	1.45 m/s	-0.05 m/s	1.01	0.99
2/14/2014	-18.3 m/s	1.05 m/s	-0.16 m/s	0.93	0.94
3/17/2014	-12.1 m/s	1.02 m/s	-0.06 m/s	0.92	0.96

Table 2.5: Tabulation of Mean Refractive Index for 1 1/2 hop scatter scenarios.

Event Date	n_1
3/3/2014	0.82
3/12/2014	0.68
3/21/2014	0.58
4/7/2014	0.68
4/10/2014	0.75
4/17/2014	0.64
4/20/2014	0.63

relatively well. The measured refractive index values for the 1/2 hop data support the theory that for quiet-time 1/2 hop ionospheric scatter, HF propagation is mostly linear.

Refractive index values may also be computed for 1 1/2 hop scatter, though the actual result may not reflect the true value due to the non-localization of 1 1/2 hop scatter propagation. Because of this, values have been tabulated in Table 2.5 using only the MoR technique. Granted, these values may not be as precise as desired, but they all illustrate a refractive index less than unity, indicating a higher degree of refractive effects than the 1/2 hop scatter. This adds further validity of using these techniques to measure refractive indices, even if just for 1/2 hop scatter.

2.4.3 Stormy 1/2 Hop Scatter Statistics

The examples previously shown for 1/2 hop ionospheric scatter focus on slow moving quiet-time scattering sources. This section presents a storm time event with 1/2 hop scatter as observed by the Blackstone SuperDARN radar. The event in question occurred on 7/14/2013 and was observed using a frequency switched mode from 6:00 UT to 10:00 UT. Figure 2.14 shows a field-of-view progression plot during the event. Examining the event in Figure 2.14 reveals a narrow channel of westward flow across the Great Lakes with velocities exceeding -400 m/s. This event demonstrates SAPS-like qualities, which is usually typified by its spatially narrow presentation, unusually high westward velocities (i.e., high polarward electric fields), and low latitude (below the auroral zone) [*Foster and Burke*, 2002]. Figure 2.15 represents the distribution of velocity values for this event. The same process as previously done on the quiet-time 1/2 hop ionospheric scatter scenarios has been applied to this storm time event. An example of the smoothed time series for beam 13 of this event is presented in Figure 2.16. The time series show a spatially limited channel with high westward velocities, very typical of SAPS-like events.

Next, we examine the time series for all beams for their velocity differences and refractive index distributions. Velocity difference values were done by subtracting the velocity magnitudes of the lower frequency content (before the switch) by the velocity magnitudes of the higher frequency (after the switch) and are presented in Figure 2.17. Much like the quiet time examples presented previously, the storm time example presents little to no velocity offset, having a mean velocity offset of only -0.06 m/s. The plot in Figure 2.18 shows the refractive index statistics for this event. The mean refractive index was found to be 0.978. Both the mean velocity offset and the mean refractive index are very similar to those values found examining 1/2 hop scatter scenarios.

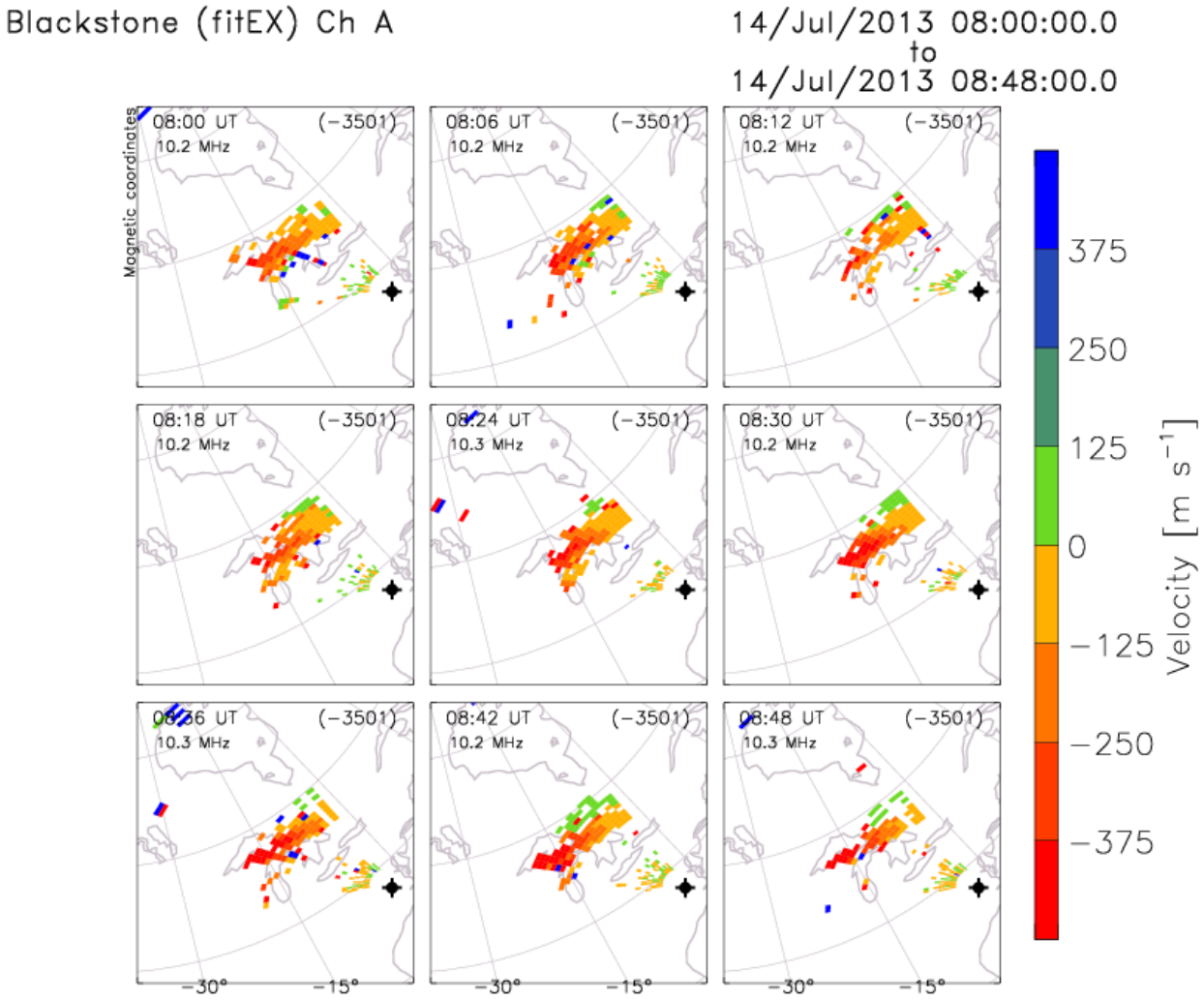

Figure 2.14: A view-of-view progression plot for a SAPS-like event occurring on 7/14/2013. The event was observed using a frequency switched mode by the Blackstone SuperDARN radar. All observations shown in this plot are on one frequency.

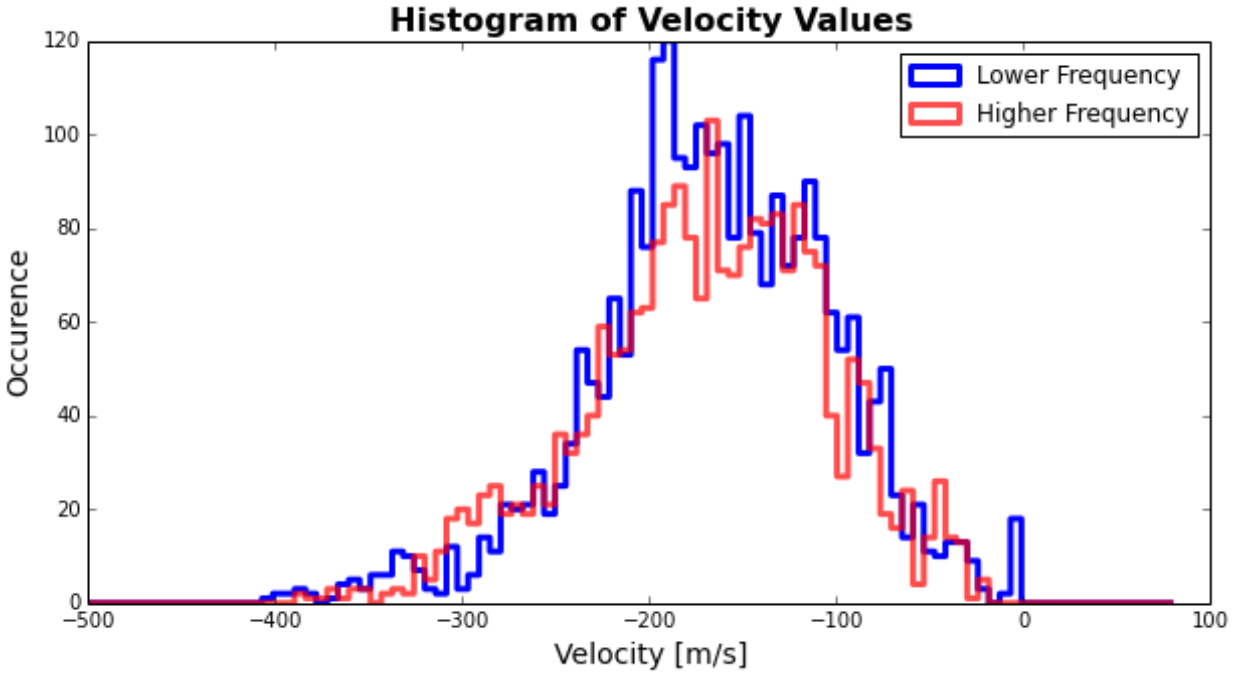

Figure 2.15: Velocity value distribution for a stormy 1/2 hop scatter scenario. The event comes from 7/14/2013. The event has a mean velocity of approximately -200 m/s.

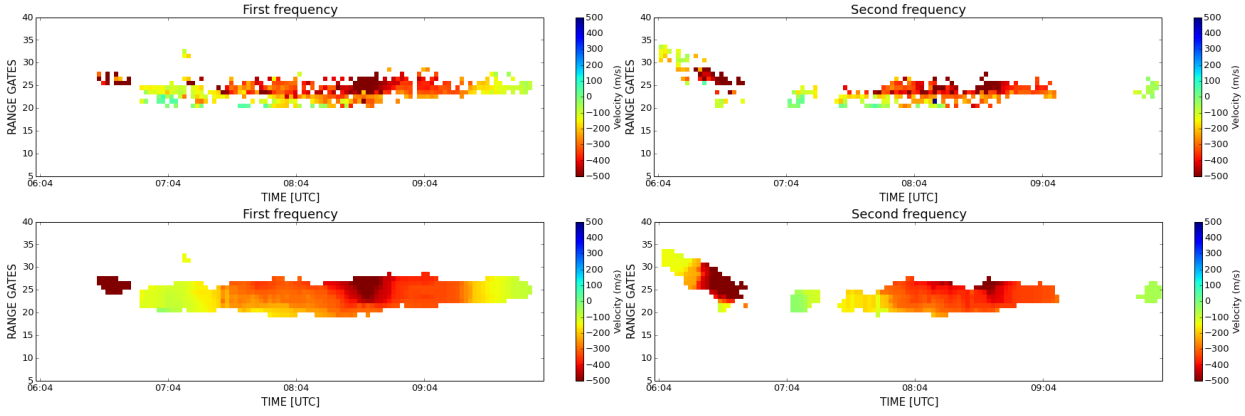

Figure 2.16: A time series example of the storm time SAPS-like event occurring on 7/14/2013. The unsmoothed velocities (top two plots) and the smoothed velocities (bottom two plots) both present velocities in excess of -500 m/s.

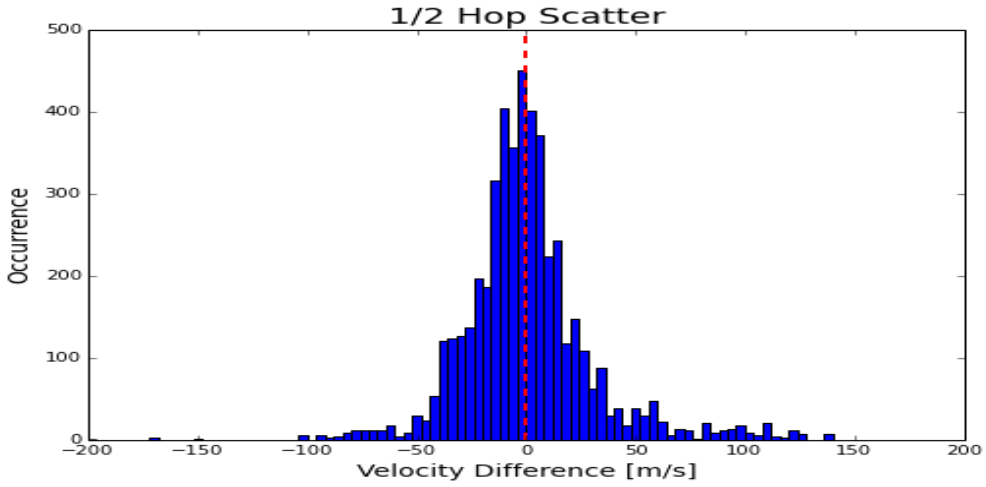

Figure 2.17: LOS velocity difference statistics for a stormy 1/2 hop scatter scenario. The event comes from 7/14/2013. The event has a mean velocity difference of -0.06 m/s, which is very similar to other quiet time 1/2 hop scatter scenarios.

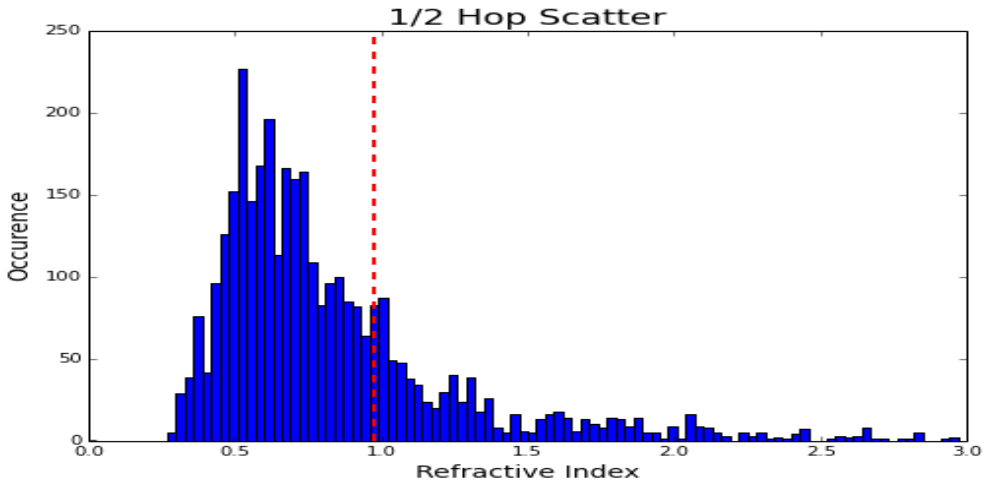

Figure 2.18: Refractive index statistics for a stormy 1/2 hop scatter scenario. The event comes from 7/14/2013. The event has a mean refractive index of 0.978, which is very similar to other quiet time 1/2 hop scatter scenarios.

This finding is significant since it means that the high velocity westward flows reported by mid-latitude radars need little to no correction factor. This is in contrast to those reports from high latitude SuperDARN radars needing correction factors as high as 20% [*Gillies et al.*, 2012]. The fact that the data shows little to no refractive influence means that the nature of mid-latitude ½ hop ionospheric scatter is most like straight line bottom side F-region [*de Larquier et al.*, 2013], though further studies should be conducted to investigate this.

2.5 Discussion

The results presented in the previous sections support the claims that the ½ hop mid-latitude ionospheric scatter is affected little by ionospheric refraction while the 1½ hop mid-latitude ionospheric scatter is greatly affected by ionospheric refraction. This result contrasts strongly with the results found in high latitude SuperDARN data [*Gillies et al.*, 2011, 2012]. Examining the results for ½ hop scatter in Table 2.3 and 2.4 reveal two important points:

a) A velocity offset between frequency switched events is essentially negligible and may not be measurable due to its small magnitude and the variability of the data.

b) Refractive index values are essentially unity (between 0.95 and 0.99), implying that the radar waves experiences little to no measurable degree of refraction.

These points validate the introductory objective statements regarding ½ hop scatter and prove the near straight line propagation nature of mid-latitude ½ ionospheric scatter. The inclusion of a storm time SAPS-like event increases the validity of the these objective statements as it encompasses all ½ hop scatter scenarios meaning the high velocities reported by storm time SAPS-like events are likely accurate, and if they are in error it is most likely

not due to refractive effects. This result is surprising given the studies claiming SuperDARN velocities are most likely underestimated. The disparity between these results and studies claiming the high influence of refraction in velocity measurements can be explained due to the locations of the studies performed. High latitude SuperDARN radars require a high degree of refraction in order to become quasi-perpendicular with magnetic field lines. This need for refraction comes with the cost of slowing group velocity, causing reported velocities to be supressed. Mid-latitude SuperDARN radars do not seem to suffer from the same problem. The inclination of magnetic field lines at mid-latitudes allows for near-straight line propagation according to raytracing [*de Larquier et al.*, 2013], and the results from this research seem to support that.

Another important point concerning the ½ hop scatter results is that the measured velocity differences in Section 2.4.1 are much smaller than the variability measured in Section 2.3. While the refractive effects seem be very close to unity, using the measured refractive values may not be appropriate. However, this does not mean that refraction should be completely neglected in ½ hop mid-latitude ionospheric SuperDARN data, it simply means a more precise method should be developed, perhaps using different instrumentation.

Examining the results for 1 ½ hop scatter in Table 2.3 and 2.4 reveal two more important points:

a) A velocity offset between frequency switched events is systematically present in 1 ½ scatter and favors a decrease in velocity magnitude as frequency increases.

b) Refractive index values are less than unity, implying that the radar waves experiences some degree of refraction.

Once again, these points validate the introductory objective statements regarding 1½ hop scatter and lend support the assumption that 1½ hop scatter may not be reliable. However,

it should be noted that the refractive indices found for the 1½ hop scatter most likely do not accurately reflect the actual refractive index of the scattering volume do the long propagation nature.

An improvement to this study would be a larger data set. The current data set consists of 12 prime examples for both ½ hop and 1 ½ hop scatter combined. The exhaustive data set does include many sub prime examples, but those are currently excluded as they are either short in time or contain strange behavior. Expanding the data set would simply required more run time and since the radar mode currently only runs on the Blackstone SuperDARN radar, expanding the radar mode to other radars would allow for the examination of geographical dependence.

Lastly, attempting to compare the results of studies like *Xu et al.* [2001] and *Drayton et al.* [2005] to mid-latitude SuperDARN radars is incorrect as it they were all done in high-latitudes. There has been a severe lack of these types of comparitive studies done at mid-latitudes, mainly due to the lack of available instrumentation. More scientific missions exploring the mid-latitude ionosphere (e.g., scientific satelites, remote sensing devices, and sounding rocket missions) would further elucidate the effects of refraction at mid-latitudes and provide a more concise answer.

2.6 Summary

This chapter has presented empirical evidence regarding the propagation of ½ hop and 1 ½ hop ionospheric scatter observed by mid-latitude SuperDARN radars. Previous studies presented evidence that high-latitude SuperDARN LOS velocity measurements may be in error due to a neglected refractive index term. This effect had not been explored at mid-latitudes. The presented results in this section are evidence ionospheric refraction has

little effect on mid-latitude ½ hop ionospheric scatter due to its near straight line nature of propagation. Conversely, the presented results prove that 1 ½ hop ionospheric scatter is strongly affected by ionospheric refraction with significant, measurable results. These results should seed future research and secure the validity LOS velocity measures of ½ hop ionospheric scatter at mid-latitudes.

Chapter 3

Conclusion/Future Work

The motivation for this research came from high latitude studies indicating a significant disparity between measured SuperDARN plasma convection velocities and those of other devices. It was found that the refractive index associated with the scattering volume was being neglected and was most likely the cause of the underestimations. This is a significant finding as the plasma convection maps provided by SuperDARN are an important tool in space weather analysis. It has been the goal is this research to explore the effects of refraction in mid-latitudes and attempt to quantify any correction needed to current and previous mid-latitude SuperDARN data.

From this motivation, it was found that nature of the observed ½ hop ionospheric scatter seen by mid-latitude SuperDARN radars is relatively unaffected by refractive effects when using a frequency switched mode. Conversely, the 1½ hop ionospheric scatter seen by mid-latitude SuperDARN radars is strongly affected. With these results in mind, it is most likely the case that no correction factor is needed for this type of scatter from these radars. If one is infact required, it does not seem to be measurable using this technique.

If it is a future studies goal to continue this work, then it would be advisable to use a larger dataset (i.e., more radars over a longer time span). Currently, the Blackstone SuperDARN radar is the only mid-latitude radar running a frequency switched mode regularly. Increased use of this mode within the mid-latitude SuperDARN community would greatly

increase the validity of these findings and lead to a deeper understanding of the refractive effects at mid-latitudes.

A different approach for this research would have been to include angle-of-arrival data in the calculation of refractive index. The Blackstone SuperDARN radar only recently began accurately collecting this kind of data, meaning a more comprehensive study may be advisable. Nevertheless, it would appear that from these results no immediate correction factor is require for mid-latitude SuperDARN velocity data.

Appendix A

Data Processing and Methods

A.1 Introduction

The variability of velocity measurements before and after a frequency shift gives insight into the refractive index due to the frequency dependent nature of the ionosphere. Accurate quantification of the background velocity variability will allow for more accurate isolation of the frequency switched velocity variability. This background velocity variability is due to multiple factors, including system noise and plasma density variation. Understanding the nature of this variability will allow for the isolation of $\mathbf{E} \times \mathbf{B}$ plasma drift velocity trends that might be missed.

The purpose of this chapter is to present the methods and techniques used in order to examine velocity variability. These techniques are used in order to remove impulsive noise from a data set, identify key features, create a continuous time series, and ultimately smooth data. The ultimate product of this process can reveal velocity trends which may have been more difficult to examine previously and allows for more accurate frequency switched velocity comparisons.

A.2 Frequency-switching in SuperDARN Radars

A SuperDARN radar typically performs a full scan every 1 to 2 minutes. A radar scan is completed when an observation has been performed on every beam sequentially and the radar is ready to begin collecting at the first beam position again. Each beam typically takes 3 to 7 seconds to process and during that time multiple pulses are sent for integration gain. During that time period, it is assumed that the targets in the illuminated scene are relatively stationary and the returns can be processed coherently. A frequency-switched mode operates by slightly adjusting the radar operating frequency between scans. An example is the SuperDARN radar in Blackstone, Virginia, which occasionally runs a mode named *twofsound* which switches between 10.3 MHz and 10.9 MHz every scan. This mode completes a scan at one frequency every 1 minute and allows for a temporal resolution of 2 minutes for each frequency. This mode began running on the Blackstone SuperDARN radar beginning April 2013 and is run sporadically due to other modes competing for time on the radar.

The purpose of this mode is to evaluate propagation characteristics between frequencies. Equation 1.11 explains that the measured LOS velocity will be a function of the refractive index of the scattering volume (e.g. the measured LOS velocity is some fraction of the $\mathbf{E}\times\mathbf{B}$ plasma drift velocity). In future sections it be revealed that the refractive index of the scattering volume is frequency dependent. With this knowledge, this mode should allow for the examination of velocity change between frequencies in order to determine characteristics of the ionosphere.

A.3 Removal of Impulsive Velocity Values

SuperDARN data is generally available at multiple levels of refinement. While it is possible to review the raw inphase and quadrature radar data, it is usually easier to interpret results after some form of autocorrelation function (ACF) fitting has been performed. A review of ACF fitting methods is given in *Ribeiro et al.* [2013] and of the two widely available formats, fitACF and fitEX, fitEX tends to give less noisy results. Despite this, fitEX SuperDARN data still tends to suffer from sporadic range bins populated with erroneous, uncorrelated velocity values. The plot in Figure A.1 demonstrates a typical quiet-time event from 2/11/2014 on beam 12. The data presented is fitEX data and represents a typical quiet-time ionospheric 1/2 hop scatter scenario. The x-axis represents dwells and the y-axis represents individual range bins. Each populated range bin represents a measured LOS velocity. It can be observed that despite the background velocity of the scatter being low, slightly negative, and well correlated, the data still contains impulsive erroneous high velocity values which stand out against background velocity values. These values will skew the dataset and must be removed.

Before the data in Figure A.1 can be processed, the data from both frequencies must be extracted and separated as these observations were made using a frequency switched mode. This can be done easily as the frequency switches back and forth every other scan. Therefore, separating every other scan yields two data sets; a dataset containing values from the first frequency and a dataset containing values from the second frequency as shown in Figure A.2. Note that when these two datasets are separated all data below range gate 7 have been removed in order to remove possible meteor scatter.

The first attempt to remove these impulsive values was the implementation of a simple SNR filter which would removal range bins below a certain power threshold as these bins may

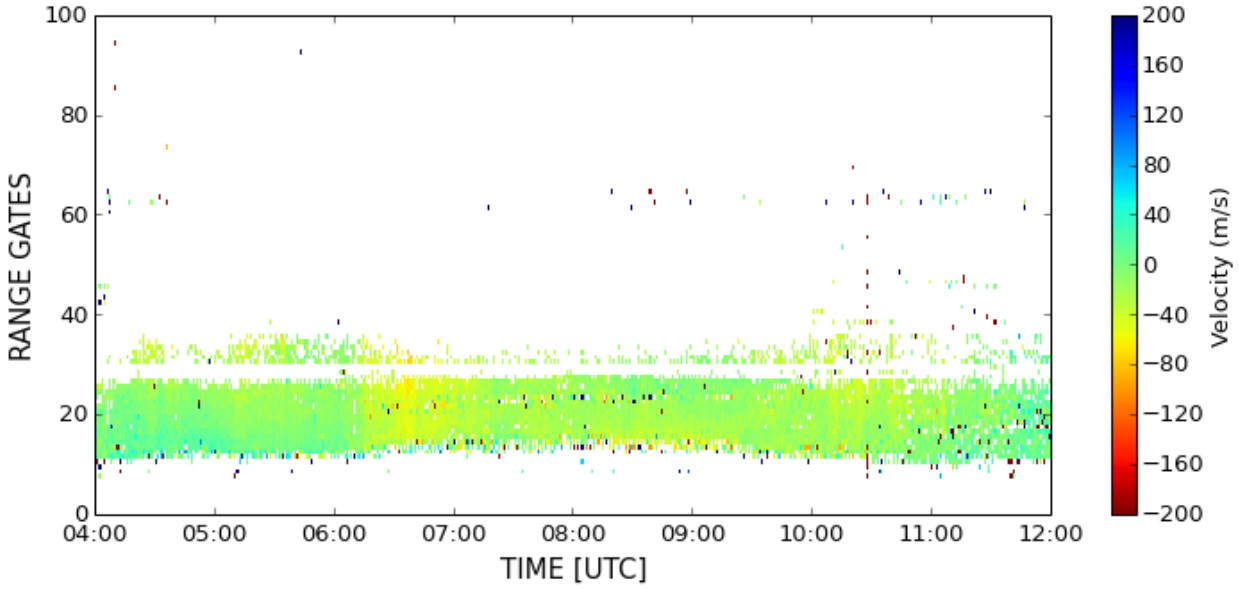

Figure A.1: Typical quiet-time fitEX velocity data (2/11/2014 on beam 12). The data is speckled with erroneous high velocity values which should be removed.

be the result of very low SNR values. This method was found to be ineffective as threshold values of even 20 dB would not remove all erroneous range bins. Another possible method would be to simply examine each image, determine a threshold for the maximum background velocity, and remove values which exceeded this threshold. This works in principle but is extremely laborious and introduces a large degree of subjectivity.

It is desirable to create a noise filter to remove these impulsive velocity values. A common technique for removing impuslive noise values from images is the implementation of an averaging filter (e.g., a linear Gaussian filter or a median filter) [*Gonzalez and Woods*, 2011]. Each output pixel is some smoothed result of all surrounding pixels. This works well against removing impulse noise values but has the effect of bleeding values into other pixels. It is important for this application to preserve the velocity values of those pixels with "true" velocities and remove those pixels with "false" velocities.

In order to remove these troublesome populated range bins, a filter was implemented

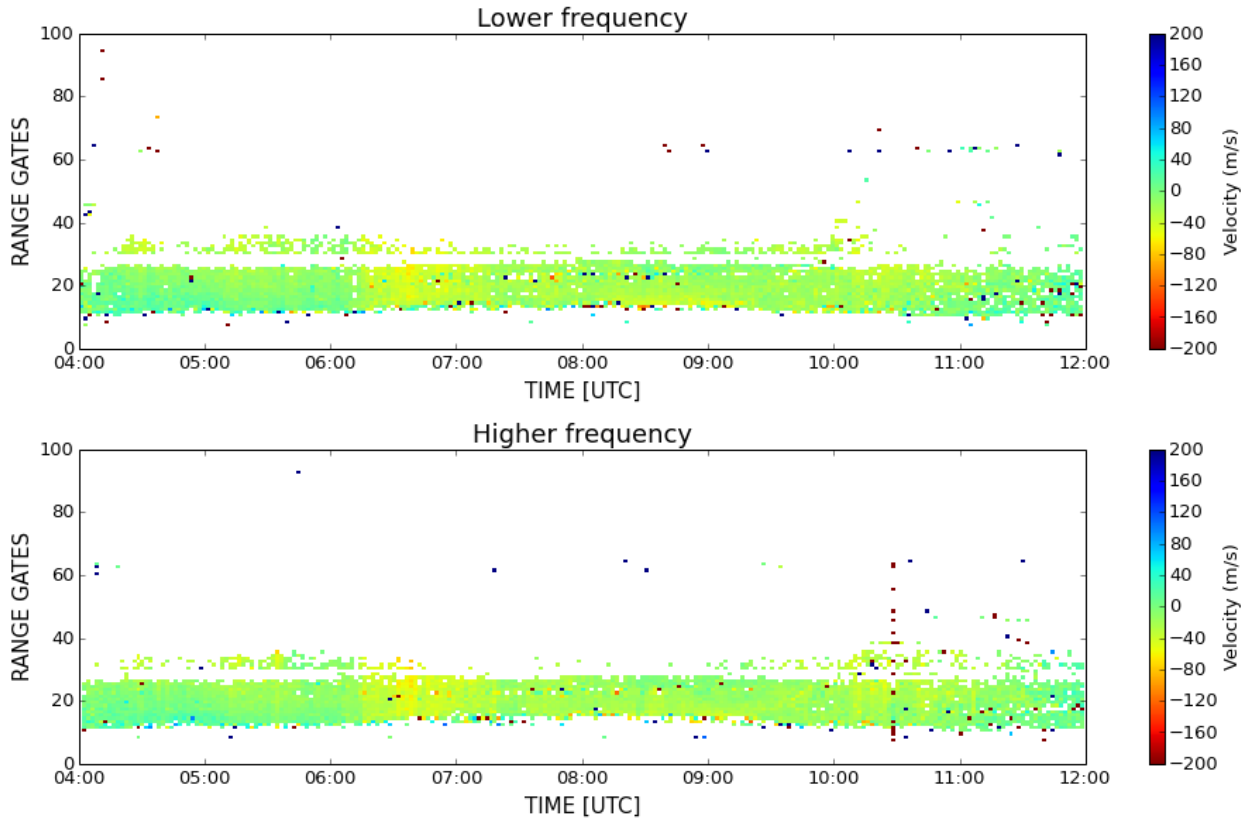

Figure A.2: Separated frequency content for the event discussed in Figure A.1. The top figure is the velocity content before a frequency switch and the bottom figure is the velocity content after a frequency switch.

which tests for uncorrelated pixel values in some defined window. In order to describe it's performance, we must first look at SuperDARN data. SuperDARN fitEX velocity data $\mathbf{V}$ can be represented in matrix form as

$$\mathbf{V} = \begin{bmatrix} v_{1,1} & v_{1,2} & \cdots & v_{1,T} \\ v_{2,1} & v_{2,2} & \cdots & v_{2,T} \\ \vdots & \vdots & \ddots & \vdots \\ v_{R,1} & v_{R,2} & \cdots & v_{R,T} \end{bmatrix} \tag{A.1}$$

where R and T are the maximum range bin and total time length of interest respectively. A typical values for R is 100, as SuperDARN radars tend have a maximum range of 4500 km. Dividing the maximum range by the common range bin size of 45 km yields 100 range bins. The value of T depends on the length of your time series and usually has time steps of around a minute. To clean the data in Equation A.1 and remove erroneous range bins, a two-dimensional filter $\mathbf{h}$ was designed with values

$$\mathbf{h} = \begin{bmatrix} 1 & 1 & 1 & 1 & 1 & 1 & 1 \\ 1 & 1 & 1 & 1 & 1 & 1 & 1 \\ 1 & 1 & 1 & 1 & 1 & 1 & 1 \\ 1 & 1 & 1 & -a & 1 & 1 & 1 \\ 1 & 1 & 1 & 1 & 1 & 1 & 1 \\ 1 & 1 & 1 & 1 & 1 & 1 & 1 \\ 1 & 1 & 1 & 1 & 1 & 1 & 1 \end{bmatrix} \tag{A.2}$$

where a is a threshold value empirically determined. The filter $\mathbf{h}$ essentially compares the sum of surrounding pixel values to the pixel in question, which has been multiplied by some threshold $-a$. By setting the threshold to the appropriate level, these values can

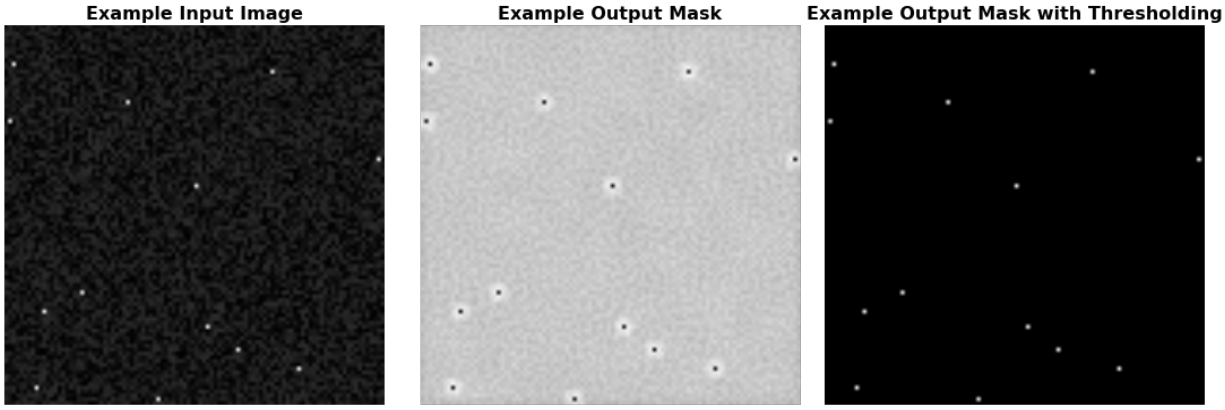

Figure A.3: A very simple example image containing well correlated random data with impulse noise values (bright white pixels). The input image (left) is correlated with a filter like $\mathbf{h}$ and the output mask is presented (middle). Note how the impulsive values stand out against background values. This can be further refined by thresholding the image so that only those uncorrelated values are present (right). This mask can be then used to find and remove impulsive uncorrelated noise values without corrupting surrounding neighbours.

be easily observed in the output image, allowing the user to remove these values from the original image. An example of the output of the filter is presented below in Figure A.3. This technique works well against slow changing image data which contains impulsive noise pixels.

The filter in Equation A.2 is correlated in both range and time with the absolute value of the fitEX velocity data represented in Equation A.1, or $\mathbf{V}_{filtered} = \text{corr}(\mathbf{V}, \mathbf{h})$. If a value in the resulting matrix $\mathbf{V}_{filtered}$ is not above some threshold then it does not correlate well with the surrounding populated range bins and is removed from the final data set. An example of effect of this filter is presented in Figure A.4 below. When compared to Figure A.2, it can be observed that the data is now much more clear which should result in more accurate average velocity estimations. It was also found that repeating this process again further increased the rejection of erroneous bins and had little effect on bins of interest. Note some scatter in higher range bins has been removed. This is beneficial as that scatter may be from E-region contamination.

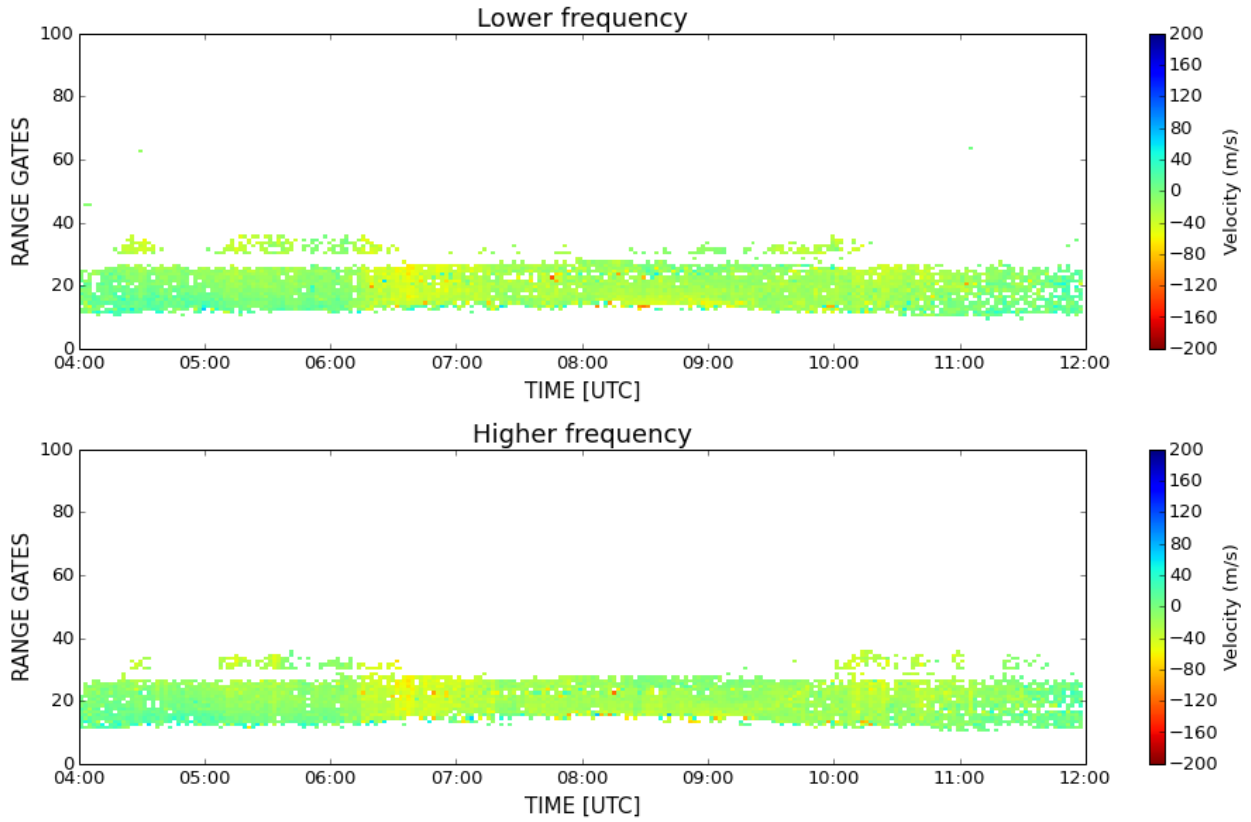

Figure A.4: Processed data from Figure A.2 after the impulsive noise filter has been applied. Note how much cleaner the data appears when compared to Figure A.2. This should allow for better localization and velocity comparisons.

A.4 Ionospheric Scatter Isolation through Blob Detection

Features of interest in SuperDARN data are usually cluttered with other content (e.g. ionospheric scatter, ground scatter, and meteor scatter in the same dwell). Isolating these features will greatly improve refractive index calculations as unwanted velocity values will be removed. In order to accomplish this, an automated blob detection algorithm was implemented.

Blob detection refers to a computer vision technique for identifying and separating regions of interest in an image. The simplest form of blob detection calculates pixel density on a per pixel basis. If some pixel does not have the required number of surrounding pixels, it is not recognized as part of a blob. More advanced techniques can be applied to this method such blob edge smoothing for better pixel inclusion and blob extraction, where blobs can be separated by desired characteristics. The blob detection technique implemented is similar to that done for cleaning the SuperDARN fitEX velocity data. A filter was created that takes into account pixel density on a per pixel basis. This filter is correlated with the fitEX velocity data and a threshold is applied to removed pixels with a low pixel density. The created square matrix filter $\mathbf{g}$ has the form of

$$\mathbf{g} = \begin{bmatrix} a_{1,1} & a_{1,2} & \cdots & a_{1,N} \\ a_{2,1} & a_{2,2} & \cdots & a_{2,N} \\ \vdots & \vdots & \ddots & \vdots \\ a_{N,1} & a_{N,2} & \cdots & a_{N,N} \end{bmatrix} \tag{A.3}$$

where N is the shape of filter and where the index values $a_{m,n}$ take the value of

$$a_{m,n} = \frac{1}{\sqrt{(N/2-m)^2 + (N/2-n)^2}}. \tag{A.4}$$

where m and n are the index of the respective row and column. Note that g is always square and N is always odd. Inspection of Equation 4 shows that the closer a pixel is to the center of the filter (i.e. the pixel of interest), the more weight that pixel has toward the total pixel density. An example of the velocity data filtered using this technique is presented in Figure A.5. Note that the velocity-scale has been enhanced in order to show finer detail. It can be observed that the detected blobs accurately represent the features of interest in the presented image and the spurious range gates which would cause velocity errors to propagate have been removed.

A.5 Data Smoothing and Empty Gate Filling

Do to the dynamic nature of the ionosphere, SuperDARN velocity data tends to contain missing range bins, or holes, in a time series. These values make analysing a complete time series difficult as they create averaging ambiguities. In order to rectify this issue, a two-dimensional median filter was implemented which ignores missing or NAN values in the over all median. This technique allows for a complete time series to be observed by sacrificing some of the finer resolution velocity data. Missing range gates which are filled are those which the blob detection found to be part of a feature but did not contain any data. Results of this implementation are presented in Figure A.6. Figure A.6 illustrates a much clear time series which will allow for the establishment of velocity trends.

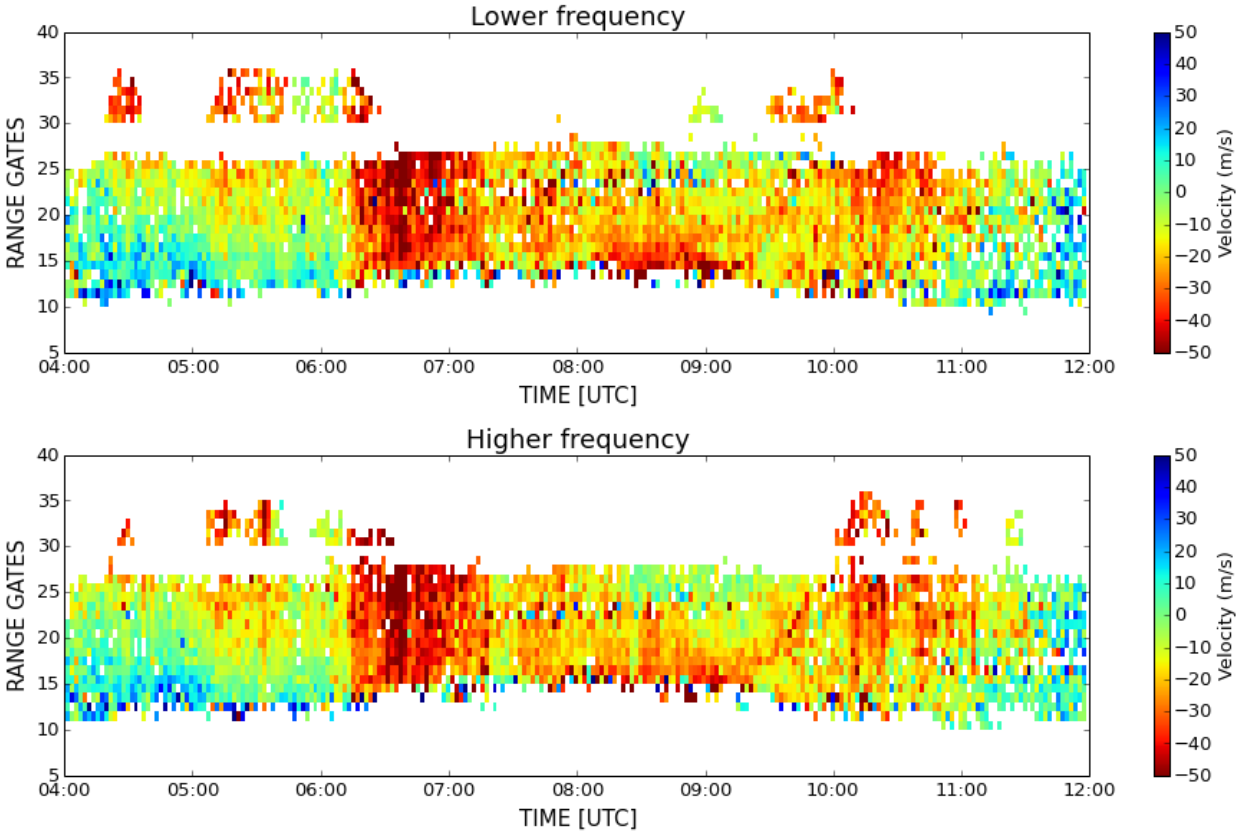

Figure A.5: Velocity data after blob detection. Comparing to Figure A.4 shows that the only remaining data is the band of ionospheric scatter of interest. Further range gates which contained possible E-region contamination have been removed. Note that the velocity scale has been increased in order to highlight detail and that the total number of range gates have been reduced in order to highlight selected features.

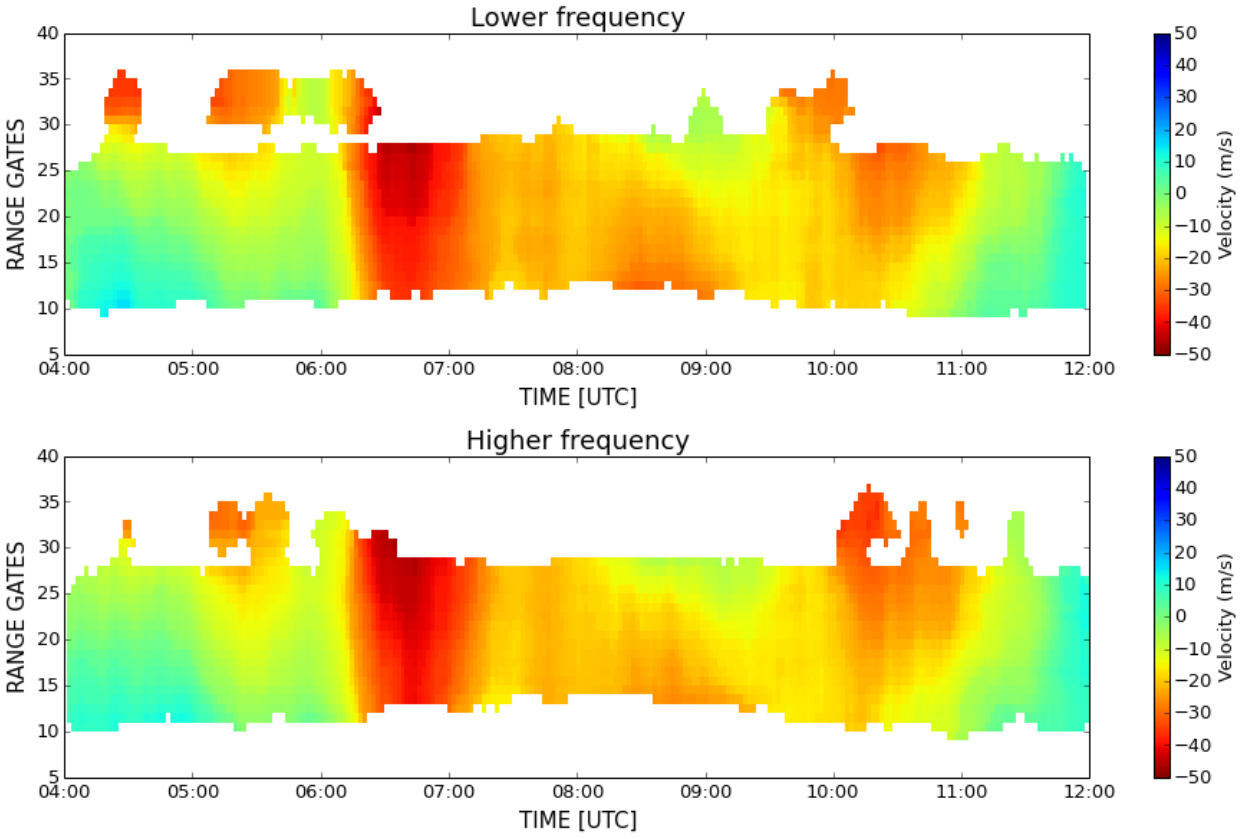

Figure A.6: Smooth velocity data. A two-dimensional median filtered is used in order to smooth velocity values as well as fill in missing values for the time series. The new time series reveals trends which may not have been easily observed at first, though some finer data has been lost.

A.6 Summary

This section has presented the methods used for processing fitEX data. These methods are implemented as it is desired to obtain a smooth time series for the velocity data. A list of the technique is as follows:

- Identify a frequency switched data set of interest. Obtain SuperDARN fitEX velocity data and check if velocity data is indeed frequency switched data. Determined frequencies used.
- Separate frequency switched velocity data into a "low frequency" data set and a "high frequency" data set based on the average frequency used. Remove first 7 range gates in order to block meteor scatter from entering the data set.
- Identify impulsive high velocity values speckling the image in order to accurately isolate lower velocity trends. Instead of using a smoothing filter technique, simply remove these values in order to not corrupt neighbouring populated range bins.
- Identify key features in the velocity data image via blob detection and remove less important structures such as E-region scatter.
- Smooth data using median filter to remove stochastic fluctuation.

The developed technique removes a degree of finer resolution information which is not pertinent to this study. The two resulting data sets allow for the easy comparison of frequency switch velocity variation.

References

H.F. Bates. A proposed polar auroral radar system. Sep 1966.

G. Chisham, M. Lester, S.E. Milan, M.P. Freeman, W.A. Bristow, A. Grocott, K.A. McWilliams, J.M. Ruohoniemi, T.K. Yeoman, P.L. Dyson, R.A. Greenwald, T. Kikuchi, M. Pinnock, J.P.S. Rash, N. Sato, G.J. Sofko, J.-P. Villain, and A.D.M. Walker. A decade of the super dual auroral radar network (superdarn): scientific achievements, new techniques and future directions. *Surveys in Geophysics*, 28(1):33–109, 2007. ISSN 0169-3298. doi: 10.1007/s10712-007-9017-8. URL `http://dx.doi.org/10.1007/s10712-007-9017-8`.

S. de Larquier, P. Ponomarenko, A. J. Ribeiro, J. M. Ruohoniemi, J. B. H. Baker, K. T. Sterne, and M. Lester. On the spatial distribution of decameterscale subauroral ionospheric irregularities observed by superdarn radars. *Journal of Geophysical Research: Space Physics*, 118(8):5244–5254, 2013. ISSN 2169-9402. doi: 10.1002/jgra.50475. URL `http://dx.doi.org/10.1002/jgra.50475`.

R. A. Drayton, A. V. Koustov, M. R. Hairston, and J. P. Villain. Comparison of dmsp cross-track ion drifts and superdarn line-of-sight velocities. *Annales Geophysicae*, 23:2479–2486, October 2005. doi: 10.5194/angeo-23-2479-2005.

J. C. Foster and W. J. Burke. Saps: A new categorization for sub-auroral electric fields. *Eos, Transactions American Geophysical Union*, 83(36):393–394, 2002. ISSN 2324-9250. doi: 10.1029/2002EO000289. URL `http://dx.doi.org/10.1029/2002EO000289`.

R. G. Gillies, G. C. Hussey, G. J. Sofko, K. A. McWilliams, R. A. D. Fiori, P. Ponomarenko, and J.-P. St.-Maurice. Improvement of superdarn velocity measurements by estimating the index of refraction in the scattering region using interferometry. *Journal of Geophysical Research: Space Physics*, 114(A7):n/a–n/a, 2009. ISSN 2156-2202. doi: 10.1029/2008JA013967. URL `http://dx.doi.org/10.1029/2008JA013967`.

R. G. Gillies, G. C. Hussey, G. J. Sofko, P. V. Ponomarenko, and K. A. McWilliams. Improvement of hf coherent radar line-of-sight velocities by estimating the refractive index in the scattering volume using radar frequency shifting. *Journal of Geophysical Research: Space Physics*, 116(A1):n/a–n/a, 2011. ISSN 2156-2202. doi: 10.1029/2010JA016043. URL `http://dx.doi.org/10.1029/2010JA016043`.

R. G. Gillies, G. C. Hussey, G. J. Sofko, and K. A. McWilliams. A statistical analysis of superdarn scattering volume electron densities and velocity corrections using a radar frequency shifting technique. *Journal of Geophysical Research: Space Physics*, 117(A8):n/a–n/a, 2012. ISSN 2156-2202. doi: 10.1029/2012JA017866. URL http://dx.doi.org/10.1029/2012JA017866.

R.C. Gonzalez and R.E. Woods. *Digital Image Processing*. Pearson Education, 2011. ISBN 9780133002324. URL http://books.google.com/books?id=MaYuAAAAQBAJ.

R.A. Greenwald, K.B. Baker, J.R. Dudeney, M. Pinnock, T.B. Jones, E.C. Thomas, J.-P. Villain, J.-C. Cerisier, C. Senior, C. Hanuise, R.D. Hunsucker, G. Sofko, J. Koehler, E. Nielsen, R. Pellinen, A.D.M. Walker, N. Sato, and H. Yamagishi. Darn/superdarn. *Space Science Reviews*, 71(1-4):761–796, 1995. ISSN 0038-6308. doi: 10.1007/BF00751350. URL http://dx.doi.org/10.1007/BF00751350.

M. C. Kelley. *The Earth's Ionosphere: Plasma Physics & Electrodynamics*. International Geophysics. Elsevier Science, 2009. ISBN 9780080916576. URL http://books.google.com/books?id=3GlWQnjBQNgC.

M. G. "Kivelson and C. T." Russell. *"Introduction to Space Physics"*. "Cambridge atmospheric and space science series". "Cambridge University Press", "1995". ISBN 9780521457149. URL http://books.google.com/books?id=qWHSqXGfsfQC.

P. V. Ponomarenko, J.-P. St-Maurice, C. L. Waters, R. G. Gillies, and A. V. Koustov. Refractive index effects on the scatter volume location and doppler velocity estimates of ionospheric hf backscatter echoes. *Annales Geophysicae*, 27(11):4207–4219, 2009. doi: 10.5194/angeo-27-4207-2009. URL http://www.ann-geophys.net/27/4207/2009/.

P. V. Ponomarenko, eJ. P. St-Maurice, J. Wiid, and M. Gillies. Two-frequency operation: pulses and minuses. 2012 SuperDARN Workshop, May 27 - June 1, 2012. PRIC, Shanghai, China, Abstracts, p. 19.

A. J. Ribeiro, J. M. Ruohoniemi, J. B. H. Baker, L. B. N. Clausen, R. A. Greenwald, and M. Lester. A survey of plasma irregularities as seen by the midlatitude blackstone superdarn radar. *Journal of Geophysical Research: Space Physics*, 117(A2):n/a–n/a, 2012. ISSN 2156-2202. doi: 10.1029/2011JA017207. URL http://dx.doi.org/10.1029/2011JA017207.

A. J. Ribeiro, J. M. Ruohoniemi, P. V. Ponomarenko, L. B. N. Clausen, J. B. H. Baker, R. A. Greenwald, K. Oksavik, and S. de Larquier. A comparison of superdarn acf fitting methods. *Radio Science*, 48(3):274–282, 2013. ISSN 1944-799X. doi: 10.1002/rds.20031. URL http://dx.doi.org/10.1002/rds.20031.

H. Rishbeth and O. K. Garriott. *Introduction to ionospheric physics*. International geophysics series. Academic Press, 1969. URL http://books.google.com/books?id=YdbAAAAAIAAJ.

M. Skolnik. *Radar Handbook, Third Edition*. Electronics electrical engineering. McGraw-Hill Education, 2008. ISBN 9780071485470. URL http://books.google.com/books?id=76uF2Xebm-gC.

R. W. Spiro, R. A. Heelis, and W. B. Hanson. Rapid subauroral ion drifts observed by atmosphere explorer c. *Geophysical Research Letters*, 6(8):657–660, 1979. ISSN 1944-8007. doi: 10.1029/GL006i008p00657. URL http://dx.doi.org/10.1029/GL006i008p00657.

Roland T. Tsunoda. High-latitude f region irregularities: A review and synthesis. *Reviews of Geophysics*, 26(4):719–760, 1988. ISSN 1944-9208. doi: 10.1029/RG026i004p00719. URL http://dx.doi.org/10.1029/RG026i004p00719.

L. Xu, A. V. Koustov, J. Thayer, and M. A. McCready. Superdarn convection and sondrestrom plasma drift. *Annales Geophysicae*, 19(7):749–759, 2001. doi: 10.5194/angeo-19-749-2001. URL http://www.ann-geophys.net/19/749/2001/.